FACULDADE DE ENGENHARIA DA UNIVERSIDADE DO PORTO


# Development of Computational Tools for Axonal Trafficking Dynamics Characterization During Electrical Acquisition and Stimulation of Neuronal Networks

**Maria João Mendes Ribeiro**

DISSERTATION

MSC IN BIOENGINEERING - BIOMEDICAL ENGINEERING

Supervisor: Cátia D. F. Lopes

Co-supervisor: Paulo de Castro Aguiar

June 28, 2020

# Development of Computational Tools for Axonal Trafficking Dynamics Characterization During Electrical Acquisition and Stimulation of Neuronal Networks

**Maria João Mendes Ribeiro**

MSC IN BIOENGINEERING - BIOMEDICAL ENGINEERING

June 28, 2020

# Resumo

O neurónio é a unidade básica do sistema nervoso sendo responsável pela rápida e precisa transmissão de sinais elétricos. A manutenção da sua estrutura e atividade é assegurada pelo transporte intracelular ao longo do axónio. Desta forma, defeitos intrínsecos ao transporte axonal associam-se a doenças neurodegenerativas, como a Esclerose Lateral Amiotrófica, que conduzem à progressiva deterioração do sistema nervoso e consequente decréscimo da qualidade de vida do paciente. Para suportar a compreensão dos mecanismos subjacentes a estas doenças e assim desenvolver métodos adequados de diagnóstico precoce e novas linhas terapêuticas, é necessário escrutinar os mecanismos que controlam a dinâmica funcional do transporte axonal e a sua relação com a atividade elétrica e transmissão de sinal ao longo da rede neuronal. Assim sendo, neste trabalho de dissertação foi usada uma plataforma que combina câmaras microfluídicas e matrizes de microelétrodos, para permitir a aquisição de imagens de microscopia de fluorescência de neurónios isolados e simultaneamente estudar a eletrofisiologia neuronal.

Esta dissertação centrou-se no desenvolvimento de ferramentas computacionais para a análise de vídeos e extração de parâmetros cinéticos do transporte axonal. Em primeiro lugar, são usadas ferramentas já disponíveis para gerar quimogramas a partir de sequências de imagens axonais e, posteriormente, foi desenvolvido um conjunto de algoritmos para segmentar automaticamente, executar regressão e extrair parâmetros cinéticos das trajetórias dos quimogramas. Esses métodos automáticos evitam a ambiguidade das inclinações selecionadas manualmente para descrever as trajetórias do quimograma e permitem extrair imparcialmente parâmetros cinemáticos. Este passo é fundamental para permitir uma caracterização mais sólida do comportamento do transporte axonal. Adicionalmente foi concebida uma interface gráfica para acesso eficiente ao algoritmo mencionado e respetivos resultados. Por outro lado, também foram desenvolvidas ferramentas computacionais para importar, visualizar e analisar dados eletrofisiológicos obtidos por matrizes de microelétrodos. O procedimento desenvolvido inclui ferramentas para avaliar a atividade neuronal, caracterizada por taxas de disparo globais e instantâneas.

Em conjunto, as ferramentas desenvolvidas estão prontas para serem usadas de forma combinada para contribuir para compreensão dos mecanismos que controlam a dinâmica do transporte axonal e a sua relação com a atividade elétrica na rede neuronal.

# Abstract

The neuron is the elementary unit of the nervous system which is responsible for the precise and rapid carriage of electrical signals. The neuronal maintenance and activity are ensured by the intracellular transport along the axon. Therefore, axonal transport defects are associated to neurodegenerative pathologies, such as Amyotrophic Lateral Sclerosis (ALS), that lead to progressive deterioration of the nervous system with a significant decrease in the patients quality of life. To support the comprehension of the underlying mechanisms of neurodegenerative diseases, and then develop adequate early diagnosis methods and therapeutic strategies, it is mandatory to reveal the mechanisms controlling the axonal transport dynamics, and its relationship with the electrical activity and signal carriage through the neuronal network. Therefore, this dissertation methodology used a platform that combines microelectrode arrays and microfluidics chamber that allows, not only the acquisition of fluorescence microscopy videos of individualized axons but also the simultaneous recording of the electrophysiological activity on the neuronal network.

This dissertation focused on the development of computational tools for time-lapse analysis and extraction of the kinetics parameters of the cargoes movement in the axon. This thesis takes advantage of already available tools to compute axonal kymographs from time-lapse movies, and develops a set of algorithms to automatically segment, perform regression and extract kinetic parameter from the trajectories in the kymographs. These automatic methods avoid the ambiguity of manually selected slopes to describe the kymograph trajectories, and allow unbiased cargoes kinematic parameters to be extracted. This is a fundamental step to provide a more solid characterization of axonal transport behavior. Moreover, it was conceived a Graphical User Interface for efficient access to the developed workflow and results. On the other hand, it was also developed computational tools to import, visualized and analyzed electrophysiological recordings obtained by microelectrode arrays. The developed procedure includes tools to evaluate the neuronal activity, characterized by global and instantaneous firing rates.

Altogether, the developed tools are ready to be used, aiding to understand the mechanisms controlling the axonal transport dynamics, and its relationship with the neuronal electrical activity.

# Agradecimentos

Em primeiro lugar endereço o meu sincero obrigada a todo o grupo NCN pela amabilidade com que me receberam e pelo espírito positivo e disponibilidade constantes. Em particular agradeço aos meus orientadores, Dra. Cátia Lopes e Dr. Paulo Aguiar, por todo o tempo e dedicação que sempre me oferecem ao longo dos últimos meses.

Quero também agradecer aos meus pais e irmã, por toda a liberdade e confiança que me deram para seguir o percurso que escolhi, e por todo o apoio ao longo da minha vida académica.

Por último, deixo umas palavras àqueles que me acompanharam nos últimos 5 anos e que tornaram o Porto um bocadinho meu. A todos os que me receberam e ensinaram a ser Engenharia e aos que eu recebi, a quem ensinei e com quem aprendi em partes iguais. A todos os elementos da Casa e aos melhores Mosqueteiros, às Clavículas e ao Baile, aos que me acompanharam nas (nada) pacíficas noitadas de trabalho e, principalmente, ao melhor grupo de miúdos que comigo entrou em 2015 e que comigo termina agora, ainda que à distância, o melhor percurso que poderia ter pedido. A todos vocês, a maior palavra de apreço por me aturarem e por fazerem de mim uma pessoa mais tolerável.

Levo-vos comigo para a vida.

Maria João Ribeiro

*"Success is walking from failure to failure*
*with no loss of enthusiasm."*

Winston Churchill

# Contents

# List of Figures

# List of Tables

# Abbreviations

| | |
|---|---|
| ALS | Amyotrophic Lateral Sclerosis |
| ANS | Autonomic Nervous System |
| AP | Action potential |
| CNS | Central Nervous System |
| CR | Contrast Ratio |
| CT | Complete Tracks |
| CTC | Cell Tracking Challenge |
| DCV | Dense core vesicle |
| DF | Difference Filter |
| DHC | Dynein heavy chain |
| DoG | Difference of Gaussian |
| DRG | Dorsal Root Ganglia |
| GUI | Graphical User Interface |
| HH model | Hodgkin-Huxley Model |
| IFR | Instantaneous Firing Rate |
| KIF | Kinesin superfamily protein |
| KHC | Kinesin heavy chain |
| KLC | Kinesin light chain |
| LAP | Linear Assignment Problem |
| LoG | Laplacian of Gaussian |
| MEAs | Microelectrode arrays |
| MPT | Mass Particle Tracker |
| MCS | MultiChannel Systems |
| NP | Number of tunable parameters |
| OP | Overall performance |
| OpenCV | Open Source Computer Vision Library |
| PNS | Peripheral Nervous System |
| ROI | Region of Interest |
| SAM | Segmentation accuracy measure |
| SAM-GT | Segmentation ground truth |
| SNR | Signal-to-noise ratio |
| SNS | Somatic Nervous System |
| SVP | Synaptic vesicle precursor |
| TF | Track fractions |
| ET | Execution time |
| TAM | Tracking accuracy measure |
| TAM-GT | Tracking ground truth |

# Chapter 1

# Introduction

The nervous system is composed of an extensive number of interacting elements including neurons and glial cells. In human, neurons from Peripheral Nervous System (PNS) could achieve over a meter long, therefore, the efficient communication between their cell body and axon tip turns to be crucial to the maintenance of neuron structure and function. The axon itself, apart from ensuring action potentials (APs) propagation, supports the supply chain of intracellular cargoes between the cell body and axon ends, to assist synaptic activity and plasticity [16].

Disturbances in the axon's physiology are behind a number of neurodegenerative diseases with high impact in our society such as Alzheimer's disease, Parkinson's disease, Huntington's disease, and Amyotrophic Lateral Sclerosis (ALS) [17]. Such diseases lead to progressive deterioration of the nervous system with a significant decrease in the patients' quality of life. They can cause partial or complete inability to carry out any everyday activity due to motor and cognitive problems, having an extensive impact at professional, social and familiar level. The increasing life expectancy accentuated the incidence of these pathologies over the years, turning neurodegenerative diseases a growing problem in developed countries [18]. In fact, the World Health Organization (WHO) predicts that by 2040, neurodegenerative diseases will overtake cancer to become the second leading cause of death after cardiovascular disease [19].

One of the most ordinary characteristics of these pathologies is the accumulation of specific proteins or damaged organelles in different types of neurons. Yet, it has been subject of the debate either such accumulations are the cause or the consequence of axonal transport defects observed in these diseases. However, it is commonly assumed that axonal transport alterations are key pathological events that contribute to neurodegeneration [15]. In recent years, some studies have provided evidence of neuronal activity-dependent regulation of axonal transport (at least for mitochondria and dense core vesicles (DCV)) [20] [21] [22] [23] [24] [25] [26] [27] [28]. These findings are still limited but so far seems to show that increased axonal electrical activity reduces mitochondrial/DCV axonal trafficking, and vice-versa.

Given the role of axonal transport disturbances in many neurological disorders, there is a pressing need to better understand them. For that, it is essential to develop experimental and technological tools that aid to scrutinize new mechanisms that can be exploited in such axon

related diseases, namely the principles behind the complex interaction between axonal transport dynamics and neuronal activity.

Therefore, this dissertation aims to contribute to this scientific need through the development of adequate computational tools that allow to accelerate such axon-related diseases studies. By using advanced in vitro models based on the combination of microElectrode arrays and microFluidic devices ($\mu EF$ platform) , neurons are able to grow their individual axons on top of microelectrodes in a compartmentalized way (i.e. the main axon segment is physically individualized from its soma and axon ends). This in vitro model provides the unique ability to combine electrophysiology, pharmacology and microscopy data and thus, achieve robust data crucial to refine the developed computational tools for the axon dynamics studies.

## 1.1 Motivation

Neuronal communication and integration in active neuronal networks depend on intracellular trafficking of several cargoes released or captured at axonal terminals. Despite its utmost importance, the principles controlling the functional dynamics of axonal transport, and its relationship with the activity of neuronal networks remain unclear. Therefore, it is essential to bring forward the research in this area and develop appropriate computational tools to assist the simultaneous study of these subjects. Afterward, it will support the discovery of neurodegenerative diseases mechanisms and allow the development of better early diagnosis and therapeutic strategies.

## 1.2 Objectives

**The main goal of this dissertation is to develop the tools that allow the characterization of the relationship between axonal transport dynamics and neuronal electrical activity**, through the use of a combined platform composed of MEAs and microfluidic devices for axonal compartmentalization. This platform allows the real-time and simultaneous electrophysiological recording/stimulation of neurons activity and the imaging of axonal cargoes trafficking.

Particularly, to fulfill the above objectives, this thesis work will encompass the development of:

- computational methodologies for image analysis of fluorescence microscopy videos to allow the extraction of axonal transport kinematic parameters.
- a graphical user interface (GUI) for easy and efficient access to the axonal transport developed methodology and results.
- a set of functions to import, visualize and analyze the activity of electrophysiological recordings obtained by MEAs.

## 1.3 Document structure

This dissertation document is structured in 5 more chapters. Chapter 2 first presents a brief description of the human nervous system organization and an overview of the main principles behind the generation of electrical signals with explanation of neuronal properties and action potential role. Then, it addresses the essential role of the axonal transport for neuronal homeostasis, detailing its machinery, velocity rate, and regulation mechanisms; the end of the section compiles the current state of the art approaches to scrutinize axonal transport dynamics and neuronal activity. The microElectrode and microFluidics ($\mu$EF) combined platform is also detailed, highlighting its importance to understand the relationship between electrophysiological recordings and axonal transport dynamics. Finally, computational methods and techniques currently used for cargo tracking are described, including image quality factors and algorithms overview with quantitative performance criteria. Two Fiji plugins algorithms are also analyzed at the end of the chapter.

Chapter 3 presents the methodology adopted to characterize the axonal transport dynamics, including the used pipeline detailing, followed by the characterization of the obtained results.

On the other hand, Chapter 4 overviews the followed approach to electrophysiological data visualization and analysis.

Finally, the main conclusions about the work developed are drawn in Chapter 5, and some future improvement suggestions are presented at the end of the document.

# Chapter 2

# Literature Review

This Chapter starts to describe the nervous system organization and the principles behind neuronal activity recordings. Then, it explores the crucial role of axonal transport, its machinery, and regulation mechanisms. Furthermore, it describes and highlights the importance of MEAs and microfluidic combined platform ($\mu$EF) for the problem in hands. Finally, it reviews the state-of-the-art computational tools for tracking cargoes.

## 2.1 Nervous System and Electrophysiology

### 2.1.1 Nervous System Organization

The human nervous system coordinates the communication between different parts of the body, controlling all essential functions of all other body systems. Concerning structural organization, the nervous system can be distinguished into two main parts, the central nervous system (CNS) which comprise the brain and spinal cord, and the peripheral nervous system (PNS), which includes the peripheral nerves (groups of axons) and ganglia (collections of cell bodies). Peripheral motor neurons carry impulses from the CNS to the rest of the body, while peripheral sensory neurons bring signals from sensory organs to the CNS [29]. The PNS is further divided into the somatic nervous system (SNS) and the autonomic nervous system (ANS). The SNS regulates the voluntary responses driving signals to the skeletal muscles. The ANS regulates the physiological and involuntary processes of the body, including the innervation of structures such as the heart, lungs (and other smooth muscles), and glands (endocrine system regulation). Moreover, the ANS is also organized into the sympathetic and the parasympathetic divisions, which operate in an opposing way to maintain homeostasis. The sympathetic system mostly produces responses to specific stimuli or stressful situations, resulting in generalized arousal. On the other hand, the parasympathetic system regulates the body at rest, in a more relaxed state [30].

The elementary unit of the nervous system, neuron (or nerve cell), is responsible for receive, process and precisely transmit electrical signals. Therefore, each neuron receives information from the environment or other nerve cells, processes the information, and sends it to other neurons or effector tissues [31]. The neuron is constituted by the cell body (typically named soma),

cytoplasm and other typical organelles. Additionally, two types of processes - axon and dendrite - extend from the soma in different number and length. Dendrites are responsible to receive and conduct electrical signals to the cell body. Contrarily, the axon is a projection specialized in the transmission of nerve impulses away from the cell body and toward other cells, through axon terminations.

Concerning the number, length and organization of its processes, the neuron is commonly classified into three different types: multipolar, bipolar, or pseudounipolar cell. Motor neurons are commonly multipolar cells with several and minor length dendrites, which form dendritic trees, and a single long axon. On the other hand, sensory neurons can be either classified in pseudounipolar or bipolar. Pseudounipolar neurons have one short common axon that splits into two branches: one branch terminates in the periphery receiving inputs from peripheral tissues, while the other branch terminates in the spinal cord where they transmit the information from the periphery. This type of neuron is found in sensory ganglia of cranial and spinal nerves. Bipolar neurons have two processes emerging from the cell body, one main dendrite that receives signals from peripheral tissues and one axon that propagates these signals to the CNS. This type of neuron is found in sensory organs, namely in the middle layer of the retina, in the olfactory mucosa, in the nasal cavity, and in the vestibular and cochlear branches of the inner ear [32].

Figure 2.1 depicted the defined neuron types.

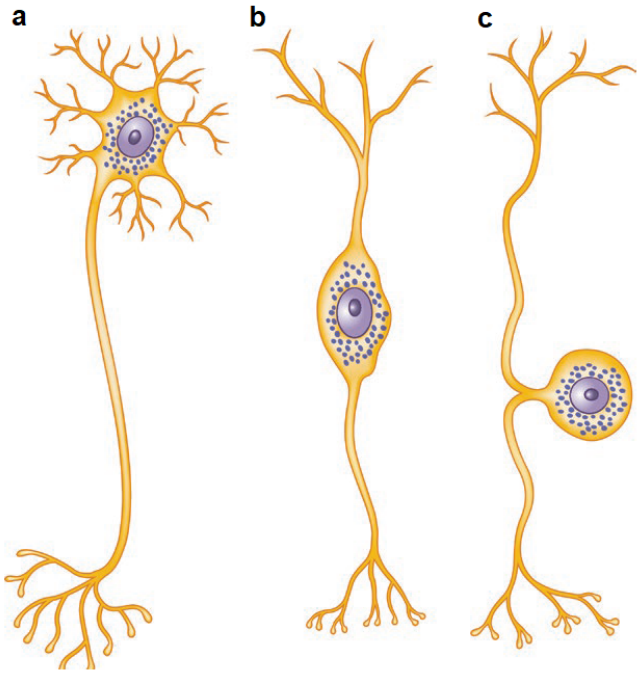


Figure 2.1: Morphological classification of neurons: (a) multipolar, (b) bipolar and (c) pseudounipolar. Adapted from [1] with permission from *Springer International Publishing*.

All neurons together form extremely organized networks for long-distance communication and information processing. The communication between neurons is conveyed by synapses, which occur between the axon of one neuron (presynaptic terminal) and the dendrites of the other (postsynaptic receptor). Synapses can be divided into two general types, electrical synapses and chemical synapses. Chemical synapses are more frequent and based their function on neurotransmitters: chemical signals messengers secreted from the presynaptic neuron. Otherwise, in electrical synapses, an ionic current flows passively through specialized cell–cell junctions - named gap junctions - which consist of clusters of double-membrane spanning hydrophilic channels (i.e. connexons) that bridge the intercellular space between adjacent cells. The space between the presynaptic and postsynaptic neurons, called the synaptic cleft, is substantially greater at chemical synapses than at electrical synapses [33].

Additionally, to increase the speed of electrical conduction, some neurons are tightly wrapped by many layers of myelin, forming myelinated axons. Myelin is a lipidic substance, which is formed by Schwann cells in PNS, and by oligodendrocytes, in CNS. Myelination occurs in a repeating sequence, with long wrapped regions (i.e. the internodes) interrupted by very short myelin-free regions called nodes of Ranvier. Therefore, the myelin acts as an insulator, reducing the leak of current through the membrane in the internodal regions, while also increasing its capacitance. Consequently, the electrical current is rapidly transported with limited loss in the internodal regions. Conduction velocity in myelinated axons is proportional to the axon diameter, while in unmyelinated axons is proportional to the square root of the axon diameter [34].

### 2.1.2 Electrophysiology

Understand the electrical communication in neuronal circuits, either in physiological or pathological conditions, is a crucial step to realize the functional dynamics of developing neuronal networks. Electrophysiology is crucial for the study of nervous system functional dynamics. It allows both the recording and modulation of neuronal activity at the single cell, but also at the network level.

Electrophysiological recordings with traditional techniques such as patch clamp, play a fundamental role in neuronal activity disclosure. However, for parallel recording, these techniques present technical limitations. Since patch clamp performs intracellular recordings (its electrodes perfuse cytoplasm), the inner composition of the cell is modified. Thus, stimulation and recording sessions have limited time to be executed [35]. Otherwise, the use of noninvasive extracellular microelectrode arrays allows the recording and stimulation of large neuronal populations for days or even months, without compromising the cell's survival. Microelectrode arrays (MEAs) technology are further explain in chapter 2.3.

Despite the electrophysiological techniques preeminence on the field, other optical methods, such as calcium imaging, are currently used to study neural activity at a cellular resolution [36]. Optical techniques are necessarily indirect, requiring, for example, calcium detectors. Therefore,

meticulous calibration is required for successful quantitative measurements. Moreover, the properties of these indicators and the uncertain quality of optical detection could reduce the temporal resolution of functional measurements [37].

#### 2.1.2.1 Neuronal Electrical Properties

To fully understand the mechanisms behind electrophysiological recording methods, it is imperative to understand the electrical properties of the neuron and its relationship with neuronal membrane dynamics. The neuron electrical properties are consequence of the different ion composition between intracellular and extracellular medium, which are separated by the cell membrane [38]. In fact, neurons are cells with a massive variety of compounds, such as inorganic ions carrying positive charge - sodium ($Na^+$), potassium ($K^+$), calcium ($Ca^{2+}$) and magnesium ($Mg^{2+}$) - and negative charge - chloride ($Cl^-$) [2].

The neuronal membrane is composed of three principal types of components that perform a crucial electrical function: the lipid bilayer itself, the embedded ion channels and pumps.

The membrane itself is composed of a 3 to 4 nm thick lipid bilayer that forms an insulator barrier for charged molecules. These two lipidic layers have hydrophobic ends pointing inwards and hydrophilic ends pointing outwards [2], establishing also a water barrier. The insulator quality causes a net build-up of differently charged ions inside and outside the membrane. It generates an electric field across the membrane, which acts as an ideal electrical capacitor.

Ions channels are pores in the membrane formed by proteins, allowing the controlled flow of ions through the lipid layer. These channels lower the effective membrane resistance, which highly depends on the density and type of ion channel. Some channels are specific to a single type of ion and do not permit the diffusion of other ion types. This selective permeability can be changed depending on the membrane potential, ionic concentrations, and extracellular concentration of bound ligands, such as neurotransmitters (for chemical synapses). Therefore, membrane properties could be comparable to ideal resistors and batteries.

Finally, ionic pumps formed also by protein structures, exchange ions against the concentration gradient with energy expending. Different pump types move a different and specific combination of ions, for example, the sodium–potassium pump exchanges two $K^+$ ions into the cell and three $Na^+$ ions out of the cell, using energy provided by the hydrolysis of one molecule of ATP into ADP and a phosphate ion [2].

Together, channels and pumps allow the flow of ions across the membrane (due to voltage changes and concentration gradients) causing a difference in the electric field between the exterior and interior of the cell, named membrane potential. This membrane potential is used to transmit long-distance signals and has its equilibrium point when the flow of ions inside the cell matches with the one outside. By convention, the extracellular medium potential is considered zero. The opening and closing of ion channels lead to potential change on ionic flow and consequently on neuron membrane potential, which may vary between -90mV and +50mV. Under resting conditions, the neuron is polarized, i.e., the excess of internal negative charge causes negative potential

(typically around -70mV). Ion pumps maintain the concentration gradient that supports this membrane potential difference [38].

#### 2.1.2.2 Action Potential: The Hodgkin-Huxley Model

Action potentials (APs) play a central role in neuron communication by providing the propagation of electrical signals along the axon. Typically, a neuron only fires an AP if its membrane potential depolarizes sufficiently to raise the defined threshold value (-55 to -50 mV). Depolarization occurs when an ionic flow leads to an acute increase in the membrane potential that rapidly achieves a peak potential of roughly +50 mV. Then, ion channels allow the positively charged ions to flow out the cell and negatively one to flow into the cell, decreasing the membrane potential (repolarization). Thus, in the hyperpolarization phase, the membrane potential falls below the resting potential before gradually recovering to the resting potential values [38].

Hodgkin and Huxley proposed a model (1952) [2] which describes the complex mechanism behind the generation and propagation of APs in neuronal membranes. Hodgkin-Huxley model (HH model) was the first one that combines successfully experimental and computational studies in neuroscience. It comprises a set of mathematical equations that explain the movement of specific particles across the membrane that are thought to control the opening and closing of sodium and potassium channels [2].

First of all, the HH model assumes the cell membrane as an equivalent circuit of a compartment, as shown in Fig. 2.2.

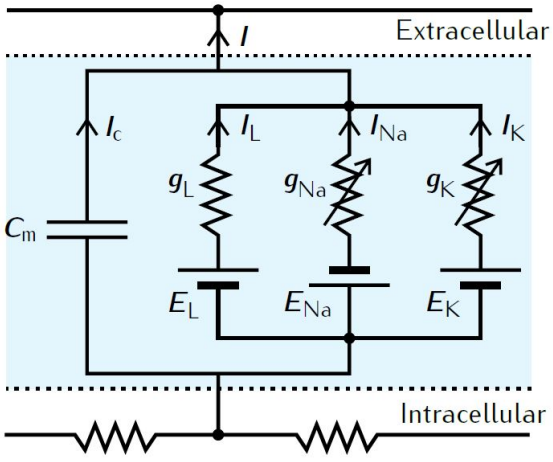


Figure 2.2: The Hodgkin–Huxley equivalent electrical circuit. Adapted from [2] with permission from *Cambridge University Press*.

Therefore, there are three types of ionic current in membrane: a sodium current, $I_{Na}$, a potassium current, $I_K$, and a leak current, $I_L$, mostly made of chloride ions. Sodium, potassium and leak conductance are expressed respectively by $g_{Na}$, $g_K$ and $g_L$ while $E_{Na}$, $E_K$ and $E_L$ are the corresponding equilibrium potentials. Finally, $C_m$ represents the membrane capacitance, $I$ the membrane current and $I_c$ the capacitive current.

The membrane equivalent circuit is define by equation 2.1, where the additional ionic current, $I_i$ is the sum of sodium, potassium and leak currents.

$$I = I_c + I_i = C_m \frac{dV}{dt} + I_i \tag{2.1}$$

As depicted in Fig. 2.2, each ionic channel is described as a battery in series with a resistance. Therefore, the intensity of each ionic current is calculated from the product of the ion's driving force and the membrane conductance for that ion. The driving force of an ion is the difference between the membrane potential, $V$, and the equilibrium potential of that ion, as stated by equations 2.2, 2.3 and 2.4. The bar on $g_L$ indicates that is a constant, while $g_{Na}$ and $g_K$ depends on the membrane potential, as indicated by the arrow over their resistors [2].

$$I_{Na} = g_{Na}(V - E_{Na}) \tag{2.2}$$
$$I_K = g_K(V - E_K) \tag{2.3}$$
$$I_L = \overline{g}_L(V - E_L) \tag{2.4}$$

Hodgkin and Huxley described ion current based on the assumption that the membrane contains several gates that can be either closed to the passage of all ions or open to the passage of potassium ions. For potassium ions to be able to flow through a gate, a number of gating particles, which control the gate, have to be in the open position. The gating particle switch between its closed and open positions can be expressed as a reversible chemical reaction, where rate coefficients depend on the membrane potential. In potassium conductance is reasonable to assume that gating particles act independently from each other. Therefore, the probability of the gate being open is $n^x$, where x is the number of gating particles in the gate, and n the independent probability of a single gating particle being open. Hodgkin and Huxley's experiments suggested that each gate is controlled by four gating particles [2], thus the membrane conductance for sodium is calculated by equation 2.5, where membrane conductance is given by the maximum conductance, $\overline{g_K}$, multiplied by the probability of a gate being open.

$$g_K = \overline{g}_K n^4 \tag{2.5}$$

Otherwise, the sodium conductance can not be described as potassium because it reaches a peak and then decays back to rest, even while a voltage remains applied to the membrane. This phenomenon is called inactivation, which is quantified with the introduction of a gating type variable, termed h. Therefore, the conductance for sodium is calculated by equation 2.6, where m represents the probability of a single gating sodium particle being active. Contrarily to potassium, experiments suggested that each gate is controlled by three gating particles [2] .

$$g_{Na} = \overline{g}_{Na} m^3 h \tag{2.6}$$

The combination of above equations result in the mathematical statement, 2.7, that represents the final model deduced by Hodgkin and Huxley to describe the membrane potential. Here $I$ represents the net contribution of the axial current from neighboring regions of the axon [2].

$$C_m \frac{dV}{dt} = -\overline{g}_L(V - E_L) - \overline{g}_{Na} m^3 h(V - E_{Na}) - \overline{g}_K n^4 (V - E_K) + I \tag{2.7}$$

## 2.2 Axonal Transport

Neurons have a large size variability with axon lengths ranging from a few microns in CNS to a meter or more in large mammals PNS, such as dorsal root ganglia (DRG) neurons. Therefore, distal termination from DRG neurons ends up to be considerably faraway from its cell body. Given that the main biosynthetic and degradative neuronal activities are centralized on the cell body, the intracellular transport along the axon turns to be crucial for the maintenance of neuron structure and function.

As a matter of fact, neurons extend their neurites and recognize the environment to make synapses with other neurons or target cells. Therefore, axonal growth and synapses are highly dependent on axonal transport for the delivery of all required proteins, lipids, RNA, and organelles that need to be transported down the axon.

On the other hand, axonal transport is also essential for the degradation or recycling of damaged and aged cellular components and organelles. Although the degradation could occur locally along the axon, more than 80% of autophagosomes move toward the cell body, indicating a dependence on axonal transport to avoid the build-up of toxic aggregates [39].

Therefore, it is evident that axonal transport is essential for neuronal maintenance, function, morphology, and survival [40]. Disruptions in the physiological dynamics of axonal transport, such as the axonal accumulation of proteins and organelles, are intimately associated with several neurodegenerative disorders. Thus, it is crucial to understand the axonal transport machinery function, regulatory mechanisms, and dynamics [17].

### 2.2.1 Axonal Transport Machinery

Axonal transport involves microtubules and the microtubule-based motor proteins - dyneins and kinesins. Microtubules consist of polarized tubulin polymers with fast-growing "plus" ends and more stable "minus" ends. In axons, microtubules are organized as unipolar arrays with "plus" ends oriented towards the axon terminals and the "minus" ends pointing to the cell body. Microtubules function as axonal rails allowing the kinesin and dynein motors to run the entire length of the axon.

The microtubules polarity confers directionality to axonal transport. Anterograde transport describes the trafficking of newly synthesized cargoes towards axon terminals (microtubule plus ends), using kinesin motors (Fig. 2.3). Retrograde transport removes aging proteins and organelles from the axon for recycling at the cell body (towards microtubule minus ends), using dynein motors (Fig. 2.3). Opposing axonal transport motors often have important biochemical and/or biophysical interactions with one another [40].

Contrarily to axons, synaptic regions such as presynaptic terminals and dendritic spines have few, if any, microtubules. At these compartments, the transport of intracellular cargoes is based on actin filaments and mediated by the myosin motors. Actin filaments are also polarized with the growing plus ends oriented towards the plasma membrane. As represented in Figure 2.3, in this

region mainly myosins convey the cargoes, serving as auxiliary function with short-range cargo movement [39].

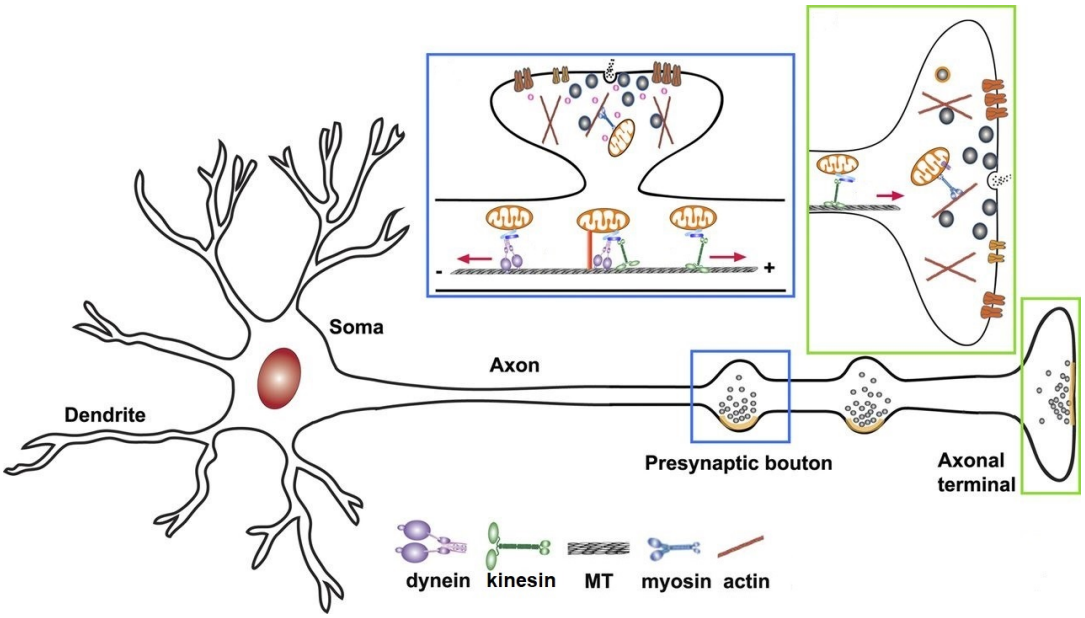


Figure 2.3: Kinesin and dynein axonal transport on microtubules and auxiliary myosins transport on actin filaments. Adapted from [3] with permission from *The Journal of Cell Biology*.

#### 2.2.1.1 Kinesin Superfamily Proteins

Kinesin superfamily proteins (KIF) are composed of a motor domain, a stalk domain, and a tail region. As represented in Figure 2.4, the motor domain binds to microtubules (moving on them by hydrolyzing ATP), whilst recognition and binding to the cargo are conduct generally by tail region, or less frequently by the stalk region [39]. In mammals such as human, there are a total number of 45 KIF genes, grouped into 14 subfamilies that share structural and functional similarities. Besides that, only motors from the kinesin-1, kinesin-2, and kinesin-3 families contribute to axonal transport dynamics [41].

Kinesin-1 motors family are responsible for the fast anterograde axonal transport of most cargoes, including vesicles, organelles, proteins, and RNA particles, as well as the slow axonal transport of cytoskeletal proteins. These motors are mostly heterotetramers composed by a dimer of kinesin heavy chains (KHCs) and a dimer of kinesin light chains (KLCs). Heavy chains comprise the motor domains and contain both ATP and microtubule-binding motifs, whilst light chains interact with the heavy chains handling cargo binding and motor activity by autoinhibitory mechanisms. Kinesin-2 and kinesin-3 motors are also crucial for regular dynamics of axonal transport: while kinesin-2 motors carry late endosomes and lysosomes, kinesin-3 motors mediate the transport of synaptic vesicle precursors (SVPs) and dense core vesicles (DCVs) [40].

#### 2.2.1.2 Dynein Superfamily Proteins

Dynein superfamily proteins include two main groups, axonemal dyneins, and cytoplasmic dyneins. Cytoplasmic dyneins move along microtubule rails by hydrolyzing ATP, being the motor responsible for retrograde transport. This protein consists of a massive complex composed of two heavy chains (DHCs) and additional intermediate, light intermediate and light chains. The carboxy terminus of DHC contains ATP and microtubule-binding motifs. The cargo-binding domain is ensured by the interaction between the amino terminus and the additional light chains. In contrast to the diversity in the kinesin superfamily, the motor subunit of cytoplasmic dynein is encoded by a single gene and has only two DHC family members [40] [41].

As represented in Figure 2.4, cytoplasmic dynein functions require an essential multi-subunit cofactor protein complex, dynactin, which regulates dynein activity and its binding capacity for cargoes.

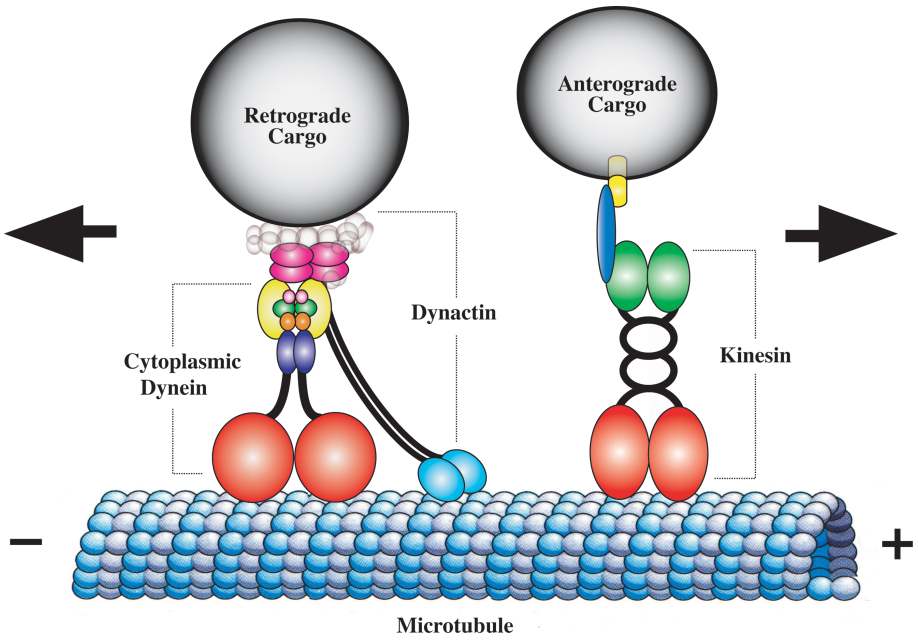


Figure 2.4: Microtubule-based cytoplasmic dynein and kinesin motors. Adapted from [4] with permission from *PLoS Genetics*.

#### 2.2.1.3 Myosin superfamily proteins

Motor proteins from myosin superfamily move along actin filaments using ATP hydrolysis to generate force. They are grouped into 18 subfamilies and perform key roles in cell movement as well as muscle contraction, cytokinesis, membrane trafficking, and signal transduction [39]. As represented in Fig. 2.5 myosins usually form a dimer and are composed by a motor domain, a neck region, and a tail region.

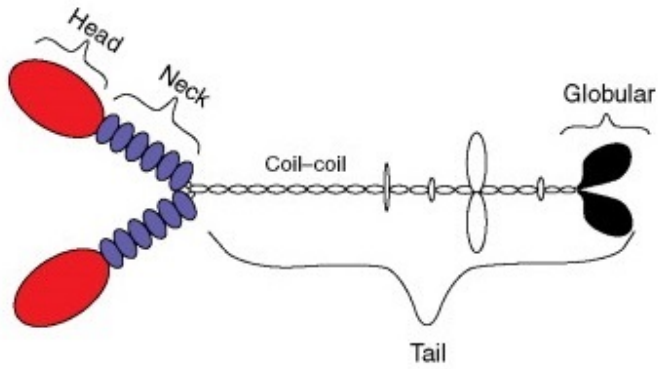


Figure 2.5: Actin-based myosin motor. Adapted from [5] with permission from *Academic Press*.

### 2.2.2 Fast and Slow Transport

The velocity of the cargoes transported in the axon is not the same for all types of structures. Axonal transport can be classified in fast or slow axonal transport. Fast axonal transport can be either in the retrograde, anterograde, or bidirectional. It is associated with the trafficking of vesicles, organelles, and RNA at speeds up to 400 mm/ day [41]. Slow axonal transport is associated with the movement of cytoskeletal polymers (e.g. neurofilaments and microtubules) and cytosolic soluble proteins along axons, at a speed less than 8 mm/day [41]. Slow axonal transport can be further classified into two subcomponents: slow component *a* (transports microtubules and neurofilaments at average rates of $\approx$ 1 mm/day) and slow component *b* (transports other proteins at average rates of 2–8 mm/day). Table 2.1 summarizes some specific transportation rates for each cargo/direction.

In recent years, studies have disclosed that the distinct rate between fast and slow axonal transport does not the result of fundamentals divergent transportation mechanisms (all cargoes are transported by the same machinery), but rather how the movement is regulated. The slow cargoes movement is indeed rapid, however, contrarily to fast cargoes, slow cargoes transportation is a balance of rapid bidirectional movements, interrupted by prolonged pauses. Thus, the main difference between both types of transport is the distinct amount of time spent in pausing. This mechanism is known as the "stop-and-go" hypothesis of axonal transport, and it has already been demonstrated for several cargoes transportation [14] [42].

### 2.2.3 Transport Regulation Mechanisms

Regulation of axonal transport occurs at multiple levels, including cargo-specific adaptors that coordinate cargo-bound motors, modulation of the microtubule tracks, and control of fast/slow transport balance.

Motor proteins are assisted by adaptor proteins, which bind motors to their cargoes and control their activity. There is an extensive amount of adaptor proteins that allows cargo recognition by the motors [39]. Motors could transport many different types of cargoes according to distinct linked adaptor protein, otherwise, the same cargo could also be transported by different motors. Recently,

Table 2.1: Motile behavior of cargoes transported in the axon. Adapted from [14] and [15]

| Moving structures | Average rate | Instantaneous rate |
|---|---|---|
| **Fast Anterograde** | | |
| Golgi-derived vesicles (containing neurotransmitters) | 200-400 mm/d (1–5 $\mu$m/s) | 2–5 $\mu$m/s (a) |
| Neurosecretory granules (containing hormones or neurotrophic factors) | 50-400 mm/d | No information |
| mRNA | 20-200 mm/d | No information |
| **Fast Retrograde** | | |
| Endocytic vesicles and lysosomes | 100–250 mm/d (1–3 $\mu$m/s) | 1–3 $\mu$m/s (a) |
| Autophagosomes | 40 mm/d | No information |
| **Bidirectional** | | |
| Mitochondria | < 70 mm/d (0.3–0.7 $\mu$m/s) | < 0.8 $\mu$m/s (a) |
| **Slow Component a** | | |
| Microtubules (Tau and Tubulin), neurofilaments | 0.2–1 mm/d (0.002–0.01 $\mu$m/s) | 0.3–1 $\mu$m/s |
| **Slow Component b** | | |
| Microfilaments (Actin), membrane proteins and enzymes | 2–8 mm/d (0.02–0.09 $\mu$m/s) | No information |

(a) The instantaneous rate is the actual rate (between pauses) determined by light microscopy. Instantaneous and average rate for fast movement are approximately the same due to lack of pausing times.

several studies have identified some of the specific motor-cargo-adaptor combinations (such as syntabulin that allows mitochondria linking to kinesin-1) and efforts have been made to scrutinize the regulatory pathway that manages the directed transport of opposing motor proteins [39] [41]. However, the mechanisms by which anterograde and retrograde movements are coordinated with one another and with stationary axonal cargoes are not yet completely understood [43].

In addition to adaptor proteins, the protein kinases also play a crucial role in the modulation of axonal transport. Kinases are ATP-dependent enzymes that, through phosphorylation (i.e. addition of a phosphate group to its proteins substrate), cause functional changes in their substrate, such as activity modification, location, or capability to associate to other proteins. Direct phosphorylation of motors, adaptors, and cargoes leads to conformational changes that cause cargo unloading or motors incapacity to bind to microtubules. Protein kinases can also indirectly control axonal transport through the phosphorylation of numerous factors required for microtubule stability, such as microtubule-associated protein tau. These changes at the microtubule level can affect motor

binding and activity [40]. Another axonal transport regulatory mechanism is the post-translational modifications of tubulin which limit the access of motor proteins to microtubule tracks in neurons [44].

The balance between fast and slow transport is also crucial to acknowledge axonal transport regulation. Different pathways have been disclosed in this subject, for instance, kinesin-1 can transport both membranous organelles (fast transport) and cytoplasmic proteinS (slow transport) depending on the interaction between the DnaJ-like domain of KLC and Hsc70 (heat shock cognate 70), which allows binding between the cytoplasmic proteins and the motor. This interaction functions as a switch between slow and fast transport [45].

Finally and specifically for mitochondria, an additional type of mechanism occurs controlling its movement over the axon. Continuous cycles of fusion and fission events aid to regulate the quality of axonal mitochondria and replenish aged organelles. Fusion in with younger mitochondria, which moves in the anterograde direction, is thought to provide essential molecules for mitochondrial survival. Otherwise, mitochondrial fission has been theorized as a mechanism to remove damaged mitochondrial components for degradation, forming a healthy organelle which continues its cycle on the axon, and an unhealthy organelle that will be further degraded [46].

### 2.2.4 Neuronal Activity and Axonal Transport Dynamics

In recent years, several state-of-the-art approaches focus on the independent study of axonal transport and neuronal activity. Although the minor percentage studies that concentrate efforts to understand the relationship between both processes, it were provided evidences of neuronal activity-dependent regulation of axonal transport.

Some of these investigations have been studied the axonal trafficking acute response to electrical stimulation. *Obashi and Okabe* [20] investigated the stability and transportation of axonal mitochondria in cultured mouse hippocampal neurons during electrical stimulation. They proposed an electrical field stimulation at 40 Hz for 10 s applied every 3 min over 50 min, by two parallel platinum wires that were mounted in a plastic lid. Their results demonstrated that mitochondrial dynamics differ between developmental stages and are regulated by neuronal activity. As a matter of fact, they concluded that average mitochondrial velocities (in both transport directions) were decreased by electrical stimulation, and mitochondrial transition from stationary to mobile seems to decreased with neuronal maturation. Otherwise, *Zhang et al.* [21] examined the interplay of calcium fluxes and mitochondrial motility in the frog, during continuous neuronal stimulation by bipolar electrodes over 2 min at 200 Hz. They conclude that the number of motile mitochondria was reduced during stimulation. To study mitochondrial trafficking along resting and electrically active adult axons, *Sajic et al.* [22] accomplished an in vivo electrical stimulation of mice's saphenous nerve at the groin, through a pair of platinum electrodes held by micromanipulators. They proposed an electrical field stimulation during 75 min ranging between 1 Hz and 50 Hz. They could observe that anterograde and retrograde mitochondrial trafficking increased in axons conducting at 1 Hz and 50 Hz versus naive animals.

Moreover, different approaches have been taken to infer the spontaneous neuronal activity of the network. *Moutaux et al.* [23] and *Ohno et al.* [24] inferred network connectivity via calcium imaging, with genetically-encoded calcium indicators, to analyze the spontaneous and synchronous activity of networks. Additionally, *Moutaux et al.* [23] also inspected glutamate transmission using a glutamate sensor that selectively measures glutamate release from glutamatergic cortical axons in GABAergic striatal neurons. Striatal neurons were therefore infected with lentiviruses expressing the glutamate sensor, and the number of fluorescent spots on striatal dendrites was counted in the synaptic chamber after chemical stimulation of cortical neurons. Although the unclear relationship between neuronal activity and synaptic formation, its estimation, through presynaptic and postsynaptic markers, was also proposed as neuronal activity indicator in broad state-of-the-art investigations, such as *Moutaux et al.* [23] and *Cagalinec et al.* [47].

Therefore, as pointed out, the reviewed literature which focuses on axonal transport interplay with neuronal activity, mainly consider indirect neuronal activity analysis, not recording directly the electrical activity of the network, through techniques such as patch-clamp or MEAs. Furthermore, these investigations offer some noticeable divergent conclusions, which confirms the emerging necessity of deepened investigation concerning axonal trafficking dynamics during electrical acquisition and stimulation.

Axonal transport is effectively characterized by its complex behavior and underlying stability processes. Thus, it is crucial to understand how axonal transport should be analyzed, i.e. what metrics we must acquire to clearly illustrate the dynamics of axonal transport. Therefore, a summary of the most extracted and reliable parameters present in the reviewed literature can be seen in Table 2.2.

Table 2.2: Commonly used parameters for axonal cargoes trafficking characterization in neurons.

| Parameter | Description | Source |
|---|---|---|
| *Stationary/motile percentage* | Graphical analysis of the evolution of axonal stationary/motile cargoes during various days in culture | [48] [23] [24] |
| *Time in motion* | For each cargo, the fraction of time it moves | [47] [48] |
| *Direction percentage* | Percentage of anterograde and retrograde transport directions | [7] |
| *Velocity* | Average cargo velocity ($\mu$m/s) when in anterograde/retrograde motion | [47] [24] [7] |
| *Peak velocity* | Maximum velocity of each cargo in specific region | [24] |
| *Number of runs* | Number of anterograde/retrograde runs per minute | [47] |
| *Run lenght* | Average length ($\mu$m) of anterograde/retrograde run | [47] |
| *Change of direction* | Change of direction during motion, described in number of turns per minute | [47] |
| *Size* | Normalized size of each cargo | [24] |
| *Velocity for heavy and light cargoes* | Distribution of transport velocities for heavy and light cargoes | [7] |
| *Linear flow rate* | The global amount of material moving | [23] |
| *Net directional flux* | The global direction of the flux | [23] |

The Linear flow rate (equation 2.8) and the Net directional flux (equation 2.9) are indirect kinetics parameters extracted using the number of anterograde/retrograde cargoes/runs ($n_a$ and $n_r$, respectively) and its velocities ($v_a$ and $v_r$, respectively):

$$\textbf{Linear flow rate} = |v_a| * n_a + |v_r| * n_r \tag{2.8}$$

$$\textbf{Net directional flux} = |v_a| * n_a - |v_r| * n_r \tag{2.9}$$

## 2.3 MEAs and Microfluidic combined platform ($\mu$EF)

As stated in Chapter 2.1, the essential process of communication in neurons is the electrical signaling, with information transmission via APs propagated along axons. Electrophysiological recordings with traditional techniques (i.e. patch-clamp) play a fundamental role in neuronal activity disclosure, but present some technical limitations (see section 2.1.2).

More recently, microelectrode arrays (MEAs) emerged with the appropriate spatial and temporal scales to access neuronal circuits, being widely used to study neuronal function in well-controlled in vitro settings. MEAs functionality relies on extracellular recordings of cells cultured on top of the electrode arrays, allowing the non-invasive recording of electrophysiological activity for long periods of time and at multiple sites [35]. Additionally, MEAs can also prompt neuronal activity by direct convey of electrical stimuli through microelectrodes [36].

Commercial available MEAs are highly versatile devices, offering varying density and size of microelectrodes, types of substrate, shapes, and geometry. MEAs must be biocompatible and tested for toxicity for prolonged periods of time and its electrodes must be composed of highly conductive metals such as gold (Au), titanium nitride (TiN), platinum (Pt), stainless steel, aluminum (Al), or alloys like iridium oxide (IrOx) [36]. These corrosion resistant microelectrodes are embedded in a glass wafer substrate that allows conventional cell culture bio-coating to improve adhesion and increase sealing resistance [49] [9]. Figure 2.6 shows an example of a commercial MEA with 256 electrodes from Multichannel Systems.

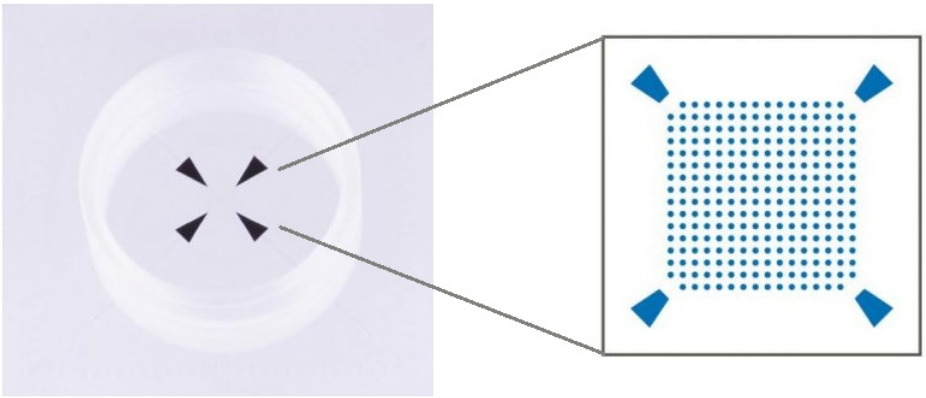

Figure 2.6: Planar 256-MEA is composed of 252 titanium nitride (TiN) recording electrodes organized in a 16 by 16 square grid, and 4 substrate-integrated internal reference electrodes. All electrodes can either be used for recording or for stimulation. Adapted from [6].

The use of MEA devices has contributed to the disclosure of the fundamental properties of neural networks, with recordings from single cells to subcellular structures such as axons. However, when compared to somal recordings, axonal recordings have a minor signal-to-noise ratio (SNR). Moreover, the MEAs capability of record extracellular field potentials from all sources around every microelectrode could become unfavorable when trying to understand communication and

signal propagation in neuronal circuits. In a network, several neurons can be simultaneously activated and generate overlapping APs, thus it became hard to track the source of the electrical signals recorded. Therefore, in these conditions source-target information is inaccessible, and the amplitudes of the APs recorded from axons are typically very low and impossible to discriminate. To overcome this limitation, the combination of microfluidics with MEAs ($\mu$EF platform) can be used to align the axonal growth within microgrooves and on top of microelectrodes and, thus improving the SNR of APs traveling along the axons [9] [50].

Microfluidic devices are very versatile in design but are generally composed of two or more cell seeding compartments, functionally interconnected by microgrooves (Fig. 2.7a for an example). When used for neuronal cultures, they allow the compartmentalization of cell bodies (and dendrites), main axon, and axon ends (Fig. 2.7b). The reduced dimensions of the microgrooves ensure that the somata (and dendrites) are excluded from these channels, whereas axons can grow through [7] [50]. Therefore, using these devices it is possible to study individualized axons into a fluidically isolated environment [51]. Such neuronal polarization, with axon isolation within microgrooves, allows to define the axonal transport direction, allowing, for instance, a clear distinction between retrograde and anterograde axonal transport [7].

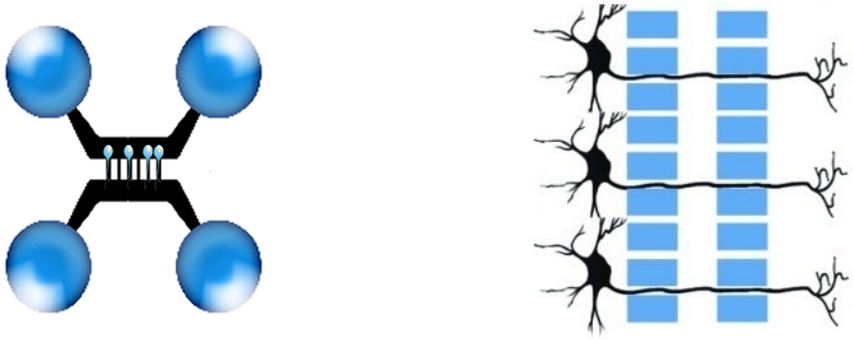

(a) (b)

Figure 2.7: Microfluid devices: (a) Microfluidic device containing mirror image cell seeding compartments connected by microgrooves. Adapted from [7] with permission from *PLOS ONE*. (b) Schematic representation of neurons compartmentalization within a microfluidic chamber, where cell bodies and dendrites are physically isolated by projecting axons and axon ends. Adapted from [8] with permission from *ACS Chemical Neuroscience*.

When microfluidic devices are combined with MEAs (uEF platforms), the microgrooves guide the growth of developing axons on top of microelectrodes, allowing the study of axonal AP propagation. To allow significant electrophysiological results, the microfluidic device must stay perfectly aligned such its microgrooves are positioned above multiple microelectrodes [50], as seen in Fig. 2.8. Furthermore, given the transparent nature of $\mu$EF substrate, it allows not only the analysis of AP propagation along the axons, but also the concomitant study of axonal transport dynamics through fluorescence microscopy techniques.

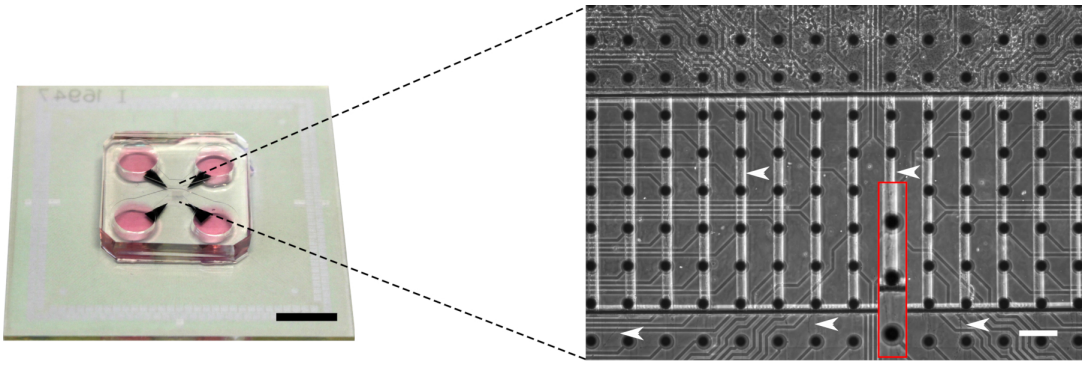


Figure 2.8: Neurons cultured on $\mu$EF platform: (a) Photograph of $\mu$EF platform. Scale bar: 1 cm. (b) Representative image of cortical neurons cultured in the $\mu$EF platform for 5 days, showing several axons crossing the microgrooves and reaching the axonal compartment (arrows). Scale bar: 100 $\mu$m. Adapted from [9] with permission from *Journal of Visualized Experiments*.

In this dissertation, one makes use of $\mu$EF platforms to study both the axonal transport dynamics and neuronal electrophysiological activity. The electrophysiological recordings were carried out using the MEA2100-System from Multichannel Systems [52]. This system is a versatile in vitro tool for extracellular electrophysiological recordings, and is composed of the following components: MEAs, headstage, interface board and PC with software, as represented in Fig. 2.9. It also includes additional elements, such as a temperature controller, an optical perfusion cannula and peristaltic perfusion pump. Although the system is compatible with different MEAs types, in this dissertation only MEAs with 256 electrodes were used.

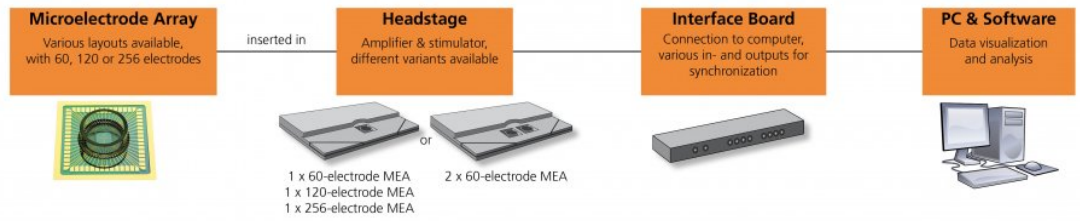


Figure 2.9: Overview of the MEA2100-System from Multichannel Systems. Adapted from [10]

The headstage is the core element of the system where MEA is lodged. Therefore, it is responsible for the signal acquisition and amplification, and to produce current or voltage stimulation signals through an integrated stimulus generator. It also allows the selection of the stimulation electrodes, permitting then to design the generated signal shape. The headstage connects to the computer through the interface board, which receives data and allow the real-time signal detection and feedback through an integrated digital signal processor. Finally, the interface board connects to the computer and software through a USB connector [10].

The MEA2100-System software package, Multi Channel Suite software supports electrophysiological data acquisition and analysis includes through three different programs: Multi Channel Experimenter, Multi Channel Analyser and Multi Channel Data manager. Multi Channel Experimenter is a data acquisition and online analysis tool that also allows to create a virtual experiment with a data source, filters, spike detection and recorder. Through this interface, the user can define acquisition parameters, such as sampling rate or stimulation electrodes, as well as, the stimulation pattern. Multi Channel Analyzer imports the data recorded with Multi Channel Experimenter and allows further offline analysis. Finally, Multi Channel DataManager assists in the progress of data exportation to analysis with third-party programs. It is able to quickly export the data into different file formats, such as *HDF5*, *.nex* or *.ced*.

## 2.4 Computational methods for tracking cargoes

Tracking cargoes is a crucial and challenging task to grant the extraction of qualitative and quantitative information about axonal transport kinetic parameters. This task involves the analysis of time-lapse images from the axon, requiring computer-vision techniques to recognize and follow cargoes across space and time.

The majority of the literature reviewed do not perform a truthful automatic cargo tracking over time. Alternatively, they mostly rely on kymograph analyses to extract kinetics parameters from microscopic videos [23] [24] [48]. A kymograph is a simple graphical method, created from time-lapse images, which displays pixel intensity values along a predefined path over time. This approach faces the computational problem of identifying corresponding particles in different frames, even on low Signal to Noise Ratio (SNR) videos with reduces particle sizes. As depicted in Fig. 2.10, kymograph generation results on 2D plots, where the vertical axis represents time and the horizontal axis represents the object position. Therefore, this method only requires the tracing of lines in an image, a much simpler task than tracking a particle over time, not only for humans but also for computational tools for automatic trajectory assignment. Static objects appear as vertical lines parallel to the time axis (their position is the same over time) while moving objects appear as easily recognizable tilted lines [53].

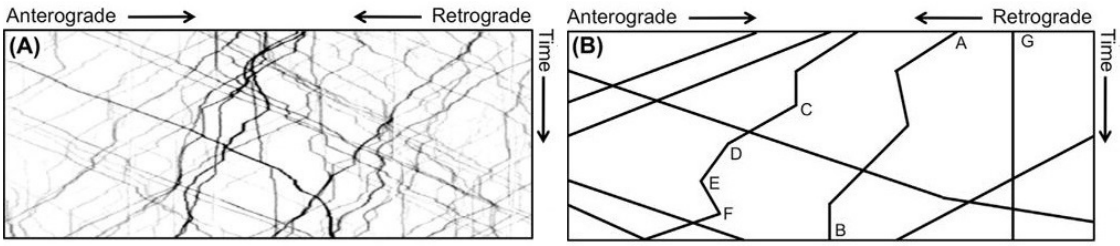


Figure 2.10: Representative kymographs for a motoneuron axon (A) and a schematic kymograph (B). Adapted from [11] with permission from *Methods in Cell Biology*.

Each line represents the track of an object (i.e. a cargo), so that measuring the lines' lengths and slopes allows the calculation of several indirect parameters, such as run-length, velocity, flux, and pause frequency [11]. Regarding Fig. 2.10.(B), the calculation of a run length can be determined for an object found in the first and last frames, such as segment A-B. Retrograde velocities can be measured for segments C-D or D-E, while the anterograde velocity can be calculated for segment E-F. Finally, a stationary vesicle is illustrated by line G. There are several software tools, such as Image J plugins, which compute kymographs from time-lapse images recordings, and then extract the desired kinetics parameters [54] [55]. More recently, *Chen et al.* [56] proposed an automatic 3D trajectory map to allow more objective analysis, less biased and with increased accuracy and sensitivity.

In complex situations, axonal transport studies require the simultaneous tracking of multiple particles whose trajectory could leave the focal plane or disappear in the background. Therefore,

these increased complexity situations present some obstacles to accurate and efficient tracking, highlighting the demand for most sophisticated methods to follow cargo movement over time.

Regarding cargoes automatic and user-independent segmentation and tracking, the structure and algorithms hereafter presented are mainly based in [12], which is a report that combines the results of three editions of the Cell Tracking Challenge [57], a competition that promotes the development and evaluation of cell segmentation and tracking algorithms. Although this initiative has not focused on axonal cargoes analysis, the same algorithms could be studied, considered, and adapted for this purpose.

At the end of the chapter, section 2.4.5 presents a brief description of state-of-the-art Fiji plugins for automatic time-lapse tracking.

### 2.4.1 Image Quality Factors

Object segmentation and tracking have variable difficulty levels depending on the quality of the recorded videos.

Segmentation comprises the accurate delineation of cargoes boundaries and is mainly affected by four quality factors: SNR/CR, heterogeneity, spatial resolution, and irregular shape. Signal to Noise Ratio (SNR), associated with Contrast Ratio (CR), measures the relationship between the signal captured from the objects and the unwanted noise capture at the same time. Microscopy images are regularly affected by noise from different sources: physiological, from the instrumentation used or from the experimental environment. Therefore, it is clear the need of image pre-processing and enhancement approaches to remove noise without loss of important information, improving the image quality [58]. Heterogeneity reflects the different average intensities between objects (inter heterogeneity) or inside an object (intra heterogeneity). Images with high intra heterogeneity could induce over-segmentation issues when each object is itself segmented into different objects [59]. A low spatial resolution could compromise the object boundary detection, and finally, irregular shape across objects may lead to both over and under-segmentation, especially in high-noise contexts.

Additionally, cargoes tracking is affected by fluorescence signal decay, temporal resolution, and split and merge events. Fluoresce temporal decay is a consequence of long-time imaging due to bleaching or quenching of the fluorochrome used to detect the target cargo type. Moreover, many algorithms rely on overlapping objects between consecutive frames to achieve precise tracking. Therefore, low temporal resolution increases the difficulty of this linking process between time-lapse images. This aspect affects even more the axonal transport tracking since several cargoes could move at different rates and with different pausing times, which complicated the simultaneous tracking of all cargoes. Finally, split and merge events, such as mitochondrial fission and fusion events, also influence tracking, requiring the correct assignment of the original mitochondria to its “daughter” on fission events, or vice-versa, on fusion events.

### 2.4.2 Technical approaches

The segmentation goal is to determine accurately every individual object region in each frame. Thus, a group of binary segmentation masks is obtained, corresponding to the object's location on a background. State-of-the-art methods commonly combine different strategies broadly classified by three criteria. Firstly, it is mandatory to analyze which detection principle is more relevant in the current image dataset. This principle could be used to find uniform areas, boundaries or bright spots and maxima. Therefore, to achieve appropriate object segmentation, it is necessary to determine which image feature will be computed, such as pixel or voxel intensity, local averages, or more complex local image descriptors of shapes or textures. Finally, there are different segmentation methods to implement the principle using the feature. These segmentation methods could be simple as thresholding, hysteresis thresholding, edge detection and shape matching, or more complex techniques like region growing, machine learning, and energy minimization.

The succeeding tracking algorithm must be able to detect moving objects, determining when the cargo appears and disappears from the focal plane. Therefore, these algorithms find the correspondence between the (segmented) masks in consecutive frames, establishing the trajectory of each cargo and even its kinetics parameters. Different tracking methods could be generally classified into two groups. Contour evolution methodologies rely on cargoes segmentation in the first frame and then evolve their contour in consecutive frames, resolving, simultaneously, the segmentation and tracking tasks. These methods assume an unambiguous spatiotemporal overlap between corresponding objects in consecutive frames. Otherwise, tracking by detection methods expect a prior object segmentation in all frames and then establish temporal associations between the segmented objects, using mostly probabilistic frameworks, such as nearest-neighbor linking, graphed-based optimization or shortest path minimization. In different scenarios, it could be used a two-frame or a multi-frame sliding window.

Figure 2.11 depicts an overview of both segmentation and tracking methodologies.

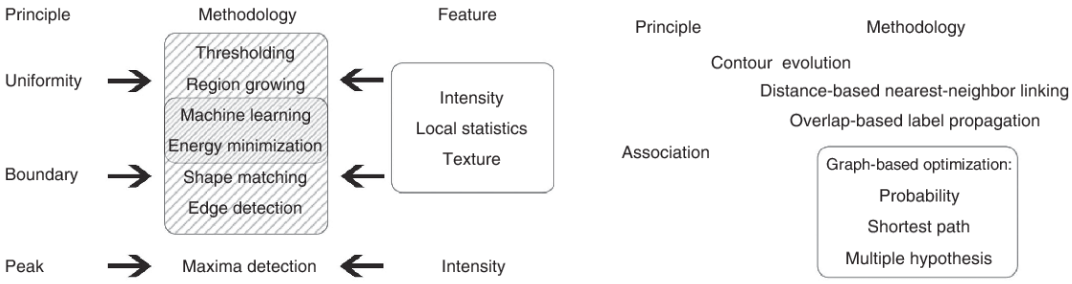


Figure 2.11: Taxonomy overview of segmentation (left) and tracking (right) methods. Adapted from [12] with permission from *Nature Methods*.

### 2.4.3 Quantitative Performance Criteria

The performance of segmentation and tracking algorithms could be quantified by three different categories of measures that evaluate the algorithm from the computer science (the developer) point of view and from the user point of view, not only evaluating the biological relevance but also the practical usability of the methods.

Generally, the first set of measures is the most relevant during algorithm development, and it is used to fine-tune the methodology. Therefore, such measures are used to highlight the superiority of new methods over current state-of-the-art methods. To perform these type of measures is mandatory the existence of a ground truth reference (for both segmentation and tracking), generally achieved manually by a specialist. The segmentation accuracy measure (SAM) evaluates the average amount of overlap between the segmentation masks computed and the reference segmentation ground truth (SAM-GT). This measure as achieved using the Jaccard similarity index, as represented in equation 2.10, where R is the reference segmentation of a cell in SAM-GT and S is its corresponding segmentation mask.

$$SAM = J(R,S) = 1 - \frac{|R \cap S|}{|R \cup S|} \tag{2.10}$$

The tracking accuracy measure (TAM) is a normalized weighted distance between the tracking solution submitted by the participant and the reference tracking ground truth (TAM-GT). Firstly, the tracking results are represented as acyclic oriented graphs, i.e., trees that capture the cell lineage during the duration of the video. Then, distance weights are assigned to reflect the effort it takes to transform manually a computed TAM into the corresponding TAM-GT, using a normalized version of the Acyclic Oriented Graph Matching (AOGM) measure (equation 2.11). $AOGM_0$ is the AOGM value required for creating the reference graph from scratch or for empty tracking results, preventing TAM from having a final negative value.

$$TAM = \frac{min(AOGM, AOGM_0)}{AOGM_0} \tag{2.11}$$

For globally rank the methodology, the overall performance (OP) is computed by averaging SAM and TAM values.

Otherwise, biologists have specific scientific questions and therefore they are usually more interested in other aspects of the final segmentation and tracking analysis. The majority of state-of-the-art parameters used to evaluate the biological relevance are focus on cell behavior and are not accurate for access the biological relevance of axonal cargoes tracking. Nevertheless, two of the parameters, complete tracks (CT) and track fractions, remain pertinent and could be adapted to the context. Complete tracks (CT) measures the fraction of ground truth object tracks that a developed algorithm can reconstruct in their entirety, while track fractions (TF) averages the fraction of the longest continuously correctly reconstructed algorithm track concerning the reference track.

Both computer science and biologically inspired measures take values in the interval [0,1], with higher values corresponding to better performance.

Finally, the practical usability of the submitted algorithms are evaluated by the number of tunable parameters (NP), its generalizability (GP) and execution time (ET). The number of tunable parameters (NP) that the user is required to manually set is the first indication of an algorithm's usability. A lower NP indicates a more usable algorithm. Otherwise, algorithm generalizability (GP) quantifies how stable an algorithm is when being applied, with the same parameter configuration, to new videos acquired under unchanged conditions. GP values are computed by comparing the results for particular training and test video and evaluating how much the result differ from one and other in terms of the technical measures (SAM and TAM). This measure takes values in the interval [0,1], with higher values corresponding to better generalizability. Finally, ET is the accumulated time, in seconds, that was required to analyze each video.

### 2.4.4 State-of-the-art Algorithms

In three Cell Tracking Challenge editions [57], several data sets for cell segmentation and tracking have been provided with two training videos with ground truth annotations and two competition (test) videos. Section 2.4.4.1 and 2.4.4.2 offer an overview of the most relevant algorithms concerning cargoes segmentation and tracking characteristics, respectively.

#### 2.4.4.1 Segmentation Algorithms

For segmentation, the overall approaches use not only pixel intensity analysis through thresholding or energy minimization, but also more complex machine learning techniques with local and texture descriptors. Machine learning techniques achieve exceptional results, but only on contrast enhancement microscopy data sets, which comprise high internal cell texture that improve the learning capacity of the algorithms. However, it is not expected that the cargoes on the axon have that distinctive texture attribute which allows accurate results.

Despite the simple approach, the most successful segmentation algorithm for the majority of data sets relies on simple intensity thresholding. Firstly, data sets are pre-processed to intensity normalization, noise suppression, and illumination correction. Binary segmentation masks are generated using a bandpass segmentation algorithm (bandpass filtering followed by thresholding), which is proceeded by a watershed transform to extract cell regions (post-processing). The filtering is performed by convolving the original image, $I$, with two different Gaussian filters $G_S$ and $G_B$ (which is much wider than $G_S$), with covariance matrices $\sum_S = \sigma_S^2 \sum$ and $\sum_B = \sigma_B^2 \sum$, where $\sum$ is the $2x2$ identity matrix. Therefore, the two filtered images are given by $I_S = I * G_S$ and $I_B = I * G_B$, and the bandpass filtered image is computed as $I_{BP} = I_S - \alpha I_B$, where $\alpha$ is a (heuristically) chosen and free parameter. The binary segmentation mask is obtained by applying the threshold $\tau$ to $I_{BP}$. This methodology includes a search algorithm for parameter optimization.

#### 2.4.4.2 Tracking Algorithms

The common denominator of almost high-performance tracking algorithms is the use of tracking by detection approach. Although, some data sets seem to endorse better results with tracking

by contour evolution algorithms, which rely on object overlapping between successive frames to achieve profitable results.

The remaining data sets end to promote better results with tracking by detection methods which are highly enriched by the use of larger, possibly global, spatiotemporal contexts, rather than look only at the nearest neighbors in space and time. The highly performance algorithm for fluorescence microscopy datasets relies on a graph-based shortest-path global optimization methodology, which considers all images of the sequence simultaneously when tracks are generated. To score different solutions to the tracking problem, this methodology introduces a set of event variables, $\varepsilon = \{\varepsilon_m\}_{m=1:|\varepsilon|}$, to represent all possible trafficking events which could occur in the image sequence. Therefore, a probabilistic scoring function has to be optimized over the iteratively adding of individual tracks to the image sequence. For each set of tracks, $F$, there is a unique set of assignments to the event variables. Then, the score of each set of tracks, $g(F)$, is defined as the sum of the logarithmic probabilities of the assignment to the individual event variables:

$$g(F) = \sum_{m=1}^{|\varepsilon|} \log(Pr(\varepsilon_m = \varepsilon_m(F))) \tag{2.12}$$

A state-space diagram is then constructed, representing all possible ways in which an additional cell track can be added to the image sequence. The change in the score, that occurs when a track is added, can be computed as the sum of the arc utilities along the corresponding path through the state space-diagram. Fig. 2.12 presents a representative state-space diagram. The scores associated with the arcs are used to find the highest scoring path, solving a shortest path problem using the Viterbi algorithm [13].

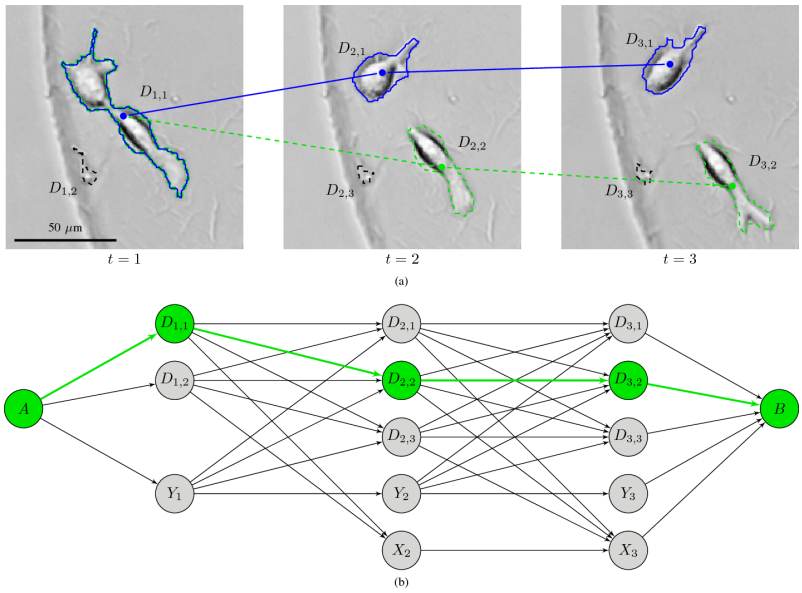


Figure 2.12: State-space diagram (b) for the addition of a track to a sequence with 3 images (a). There is a preexisting track shown in blue, and the state-space diagram describes all the possible ways to add a second track. The arrows that go out of "X" states , represent new objects into the field of view, while, the arrows that go into the "Y" states represent objects that disappear from the field of view. Adapted from [13] with permission from *IEEE transactions on Medical Imaging*.

This tracking algorithm was developed by the same team of the already introduced segmentation algorithm, which supports the fact that the tracking algorithm performance seems to be heavily influenced by the performance of the segmentation approach. Therefore, for successful object tracking it is mandatory a high-performance segmentation algorithm with appropriate parameters for a given data set. The global algorithm has been developed in MATLAB and are available through the CTC website [60], along with correspondent executable version and parameters used to produce the submitted results.

From the user perspective, a complete and perfect unsupervised segmentation and tracking methodology remain unsolved since state-of-the-art algorithms continued to have a large number of tunable parameters and required pre and post-processing work.

### 2.4.5 Fiji Plugins

Fiji is an open-source distribution of ImageJ that includes a great variety of organized libraries and plugins, relevant for biological research, as well as, scripting languages, extensive tutorials, and documentation. This tool combines modern software engineering practices to enable rapid prototyping of image-processing algorithms, especially focused on biomedical image analysis [61]. Among the large set of Fiji plugins, there is a specific category focus on object tracking, including plugins such as TrackMate and Difference Tracker.

#### 2.4.5.1 TrackMate

TrackMate is an openly available and well-documented tracking plugin that includes several detection and tracking modules, combining manual and automated particle tracking approaches. It is a user-friendly solution that includes several visualization tools and tailored solutions. TrackMate also allows further analysis with other tools, including features to extract files with relevant data and results [62].

Before any processing, TrackMate offers the possibility to use a 3x3 median filter to help dealing with salt and pepper noise. For cargoes segmentation, this plugin offers five different methodologies to detect all individual objects in each frame. Apart from Manual Annotation, where it is possible to manually select the target objects, there are four more detectors all based in Log Filter: LoG detector, DoG detector, downsample LoG detector and block LoG detector. Laplacian of Gaussian (LoG) detector focuses on local maxima, applying a simple Laplacian of Gaussian filter. The filter standard deviation is tuned according to the object radius, which is entered by the user. All calculations are made in the Fourier space, which makes it optimal for spot diameters between 5 and 20 pixels. The difference of Gaussian (DoG) detector reproduces the LoG detector logic, approximating it by the difference of two Gaussians. Calculations are made in the direct space, and it is optimal spots with diameters below 5 pixels. The downsample LoG detector has been conceived to handle larger objects, downsizing the image by an integer factor before LoG detector filtering. This makes it optimal for large spot sizes, above 20 pixels in

diameter. Finally, the block LoG detector splits the image into small blocks to limit memory usage in the case of a large input image [62].

Just after this filtering step, object features such as mean, median, min, max and total intensity are calculated, as well as, its standard deviation, contrast, and diameter. Accordingly to user choice, these features are used to select target objects, based on selected filter type set to retain only objects with a given feature below or above a specified threshold.

Then, there are four particle-linking algorithms that connect filtered spots to build tracks. For object linking, it is also available the option to skip the automatic tracking and use the manual approach. Apart from that, in TrackMate, the LAP (Linear Assignment Problem) methodology supports three different tracker approaches, the LAP tracker, the Simple LAP tracker and the linear motion LAP tracker. The LAP tracker is prepared to handle different imaging events, such as split, merge and gap closing events (when an object disappears from the focal plane and then reappears a bit further). Simple LAP tracker is just a simplified version of the first one with fewer settings and only deal with particles which do not divide nor merge. All the linking costs for these two trackers are based on the particle-to-particle square distance. A cost matrix is computed containing all possible assignment costs, and then the LAP algorithm returns the list that minimizes the sum of the costs, which could be tuned by adding penalties on spot features. Therefore, the user is asked not only for a maximal allowed linking distance but also for possibly spot features and correspondent penalty weights. Otherwise, the linear motion LAP tracker simplifies the method described and it is only suitable for tracking particles that move with a roughly constant velocity. Finally, the Nearest neighbor search tracker presents a simple algorithm to spot tracking. The user sets only a maximal linking distance, and then each spot in one frame is linked to another one in the next frame, achieving only a very local optimum [62].

The main achievement of this plugin focuses on particle tracking, and therefore its results take the shape of tracks, collections of spots and links. TrackMate also offers basic track visualization tools plotting several types of features (velocity, length, duration, etc) as a function of another. However, specific applications, like axonal transport analysis, require a refined analysis, which demands TrackMate files to be interpretable for specialized software. Therefore, TrackMate documentation [62] describes, in detail, several ways of importing TrackMate data in specialized tools such as MATLAB or Python, explaining how to deal with complex tracks and showing examples of basic analysis and visualization.

TrackMate has been already used to axonal transport tracking producing kinetic parameters similar to the ones achieved by manual tracking [63].

#### 2.4.5.2 Difference Tracker

Difference Tracker [64] is a software tool that combines two ImageJ plugins, Difference Filter (DF) and Mass Particle Tracker (MPT), to provide fast and fully automated analysis of particle movement. This software was conceived to aid in the comparative analysis of axonal transport in

different situations. It could identify and track multiple motile particles simultaneously in time-lapse images, returning values for several kinetics parameters. Difference Tracker is released as free software and could be optimized further to report additional transport parameters.

The Difference Filter (DF) plugin performs an independent difference filtering on each pixel of every frame. The difference is calculated between a user-defined number of offset frames. Only positive changes in pixel intensity are retained to the avoid generation of "shadow" particles. To identify all pixels in a given motile particle, it is mandatory to set an offset value sufficiently high to allow the whole particle movement to a non-overlapping position. Therefore, the DF identifies moving particles, and filters out stationary ones together with background noise, providing a simple set of frames which simplifies the following MPT plugin tracking.

The Mass Particle Tracker (MPT) plugin is used to track moving particles after the moving pixels isolation by the DF plugin, or, in simple situations, directly in time-lapse images. This plugin performs threshold-based detection on each frame, characterizing adjacent pixels and merging them into features (each feature representing a particle). Then, features are linked into tracks, finding, consecutively, the closest feature in the following frame. When a track starts, the movement between the last two frames is projected to provide a prediction of the feature position in the next frame. A track finish when it can not link with a feature in the next frame. Otherwise, if there are no existing tracks to link to a feature, a new track is created.

Difference Tracker does not assume gap-closing events, i.e. the algorithm does not make assumptions about the cargo route when it momentaneous disappears and reappears later. Thus, the plugin finishes the track and initiate a new one when the particle reappears. Furthermore, Difference Tracker neither detects nor tracks stationary cargos. Therefore, several parameters associated with these cargoes quantification are not included in statistics returned by the plugin. However, [64] assumes that the behavior of stationary cargoes could be inspected through the analysis of the particle count variation since the overall reducing of cargoes movement would indicate the pausing times increasing.

Statistic parameters reported from both DF and MPT plugins are automatically recorded in a text file which can be exported for further statistical analysis. The data extracted include total track count, average motile particle per frame, average track duration, average particle size, average speed per track, and maximum speed per track. An annotated version of the time-lapse images is also made available with all tracked cargoes highlighted, allowing the quality analysis of the tracking performance. The MPT plugin could also extract the coordinates of each individual tracked cargo in each frame.

# Chapter 3

# Axonal Transport Analysis

As stated in Section 2.2 the axonal transport characterization is a crucial task while studying neuronal networks and its maintenance, function, and survival. As a matter of fact, several neurodegenerative diseases are associated with axonal transport disorders consequently, the discovery of its regulation mechanisms could contribute to the development of better early diagnosis or therapeutic strategies.

One of this dissertation goals is to develop the tools that allow the characterization of axonal transport dynamics. Therefore, this chapter describes the methodology developed to analyze axonal transport dynamics through video recordings of DRG explants cultures on platforms. It first overviews the methods carried out to analyzed axonal transport, including a brief description of the experimental setup, the applied video registration algorithm, and the explanation of the developed approach to kymograph segmentation and analysis. Additionally, it explores and discusses the kinematics parameters extracted from kymographs and presents a graphical user interface developed for easy and efficient access to the developed segmentation algorithm and results.

## 3.1 Methods

### 3.1.1 Experimental Setup

#### 3.1.1.1 Microfluidic chambers preparation

Microfluidic chambers were prepared by placing the microfluidic devices against a pre-coated glass coverslip, as previously described [65]. In brief, the coverslips were coated with 0.01 mg/ml of poly(D-lysine) (PDL, Corning), overnight at 37 °C. Microfluidic devices were sterilized with 70% ethanol and were gently attached to the PDL-coated coverslips, creating a microfluidic chamber composed of two separate cell seeding compartments connected by microgrooves. The cell seeding compartments were then loaded 5 $\mu g/ml$ laminin isolated from mouse Engelbreth-Holm-Swarm sarcoma (Sigma-Aldrich Co.) and incubated overnight at 37 °C. The unbound laminin-1 was removed, and the chambers were refilled with culture medium and left to equilibrate for at least 2 h at 37 °C prior to cell seeding.

#### 3.1.1.2 DRG explant culture

Experimental procedures involving animals were carried out in accordance with current Portuguese laws on Animal Care (DL 113/2013) and with the European Union Directive (2010/63/EU) on the protection of animals used for experimental and other scientific purposes. The experimental protocol (reference 0421/000/000/2017) was approved by the ethics committee of the Portuguese official authority on animal welfare and experimentation (Direção-Geral de Alimentação e Veterinária). All possible efforts were made to minimize the number of animals and their suffering. Unless otherwise stated, all reagents listed below are from Gibco, Thermo Fisher Scientific. Primary embryonic rat DRG explants were isolated from Wistar rat embryos (E18). Lumbar DRG explants were removed and placed in Hank's Balanced Salt Solution (HBSS) until use. Upon use, one DRG explant was seeded in the cell body compartment of a microfluidic chamber, previously treated with 0.01 mg/ml PDL plus laminin as described in Section 3.1.1.1. Cells were cultured in DMEM/F12 medium supplemented with 2% B27, 50 ng/ml of NGF-7S (Sigma Aldrich Co.), and 1% penicillin/streptomycin (P/S, 10,000 units/ml penicillin and 10,000 $\mu$g/ml streptomycin), and kept in a humidified incubator at 37 °C supplied with 5% $CO_2$.

#### 3.1.1.3 Mitochondria labelling and live imaging

At day in vitro (DIV) 6, DRG neurons were incubated with 50nM MitoTracker® Orange (Thermo Fischer Scientific) under normal culture conditions for 45 minutes. Cells were live-imaged in the day after using a fluorescence microscope Eclipse Ti2 (Nikon) connected with a Prime 95B camera (Photometrics). Imaging was performed at 37°C under a 5% CO2 atmosphere, using a 40X water objective. Laser line at 532 nm was used for excitation.

Microgrooves (containing at least one axon) were randomly selected for live imaging. All image series were acquired at 5 Hz for 5 minutes. This interval of seconds between frames allowed for long-term imaging without dye bleaching. The original acquired videos included several microgrooves imaged in the same recording. To aid in the further analysis, all recordings were split using Fiji, obtaining a normalized set of videos with a single microgroove.

### 3.1.2 Video Registration

During image acquisition, some instability on the recording system installed on the microscope leads to the camera motion and consequent movement of the field of view. Therefore it is imperative to perform a video registration, stabilizing all frames in the same coordinate system to allow the integration of the data obtained from the different frames.

Video Stabilization is then achieved through a Point Feature Matching approach, which detects feature points in the reference and input frames, estimates the motion between them, and tries to align the global field of view.

The high temporal resolution of the sequence recorded leads to a sub-pixel motion level between consecutive frames. Therefore, before any processing, it was performed an image interpolation to increase image size and adjust the motion to pixel resolution. After the stabilization algorithm, all frames were interpolated back to the original size.

In this thesis work, six drifting individual microgrooves videos (where axonal cargoes movement is visible) were stabilized using the further explained point feature matching technique. The registration algorithm was implemented using Python programming language and the well-documented Open Source Computer Vision Library (OpenCV).

Figure 3.1 depicts the overview of the implemented steps of video registration that will be described further ahead in this section.

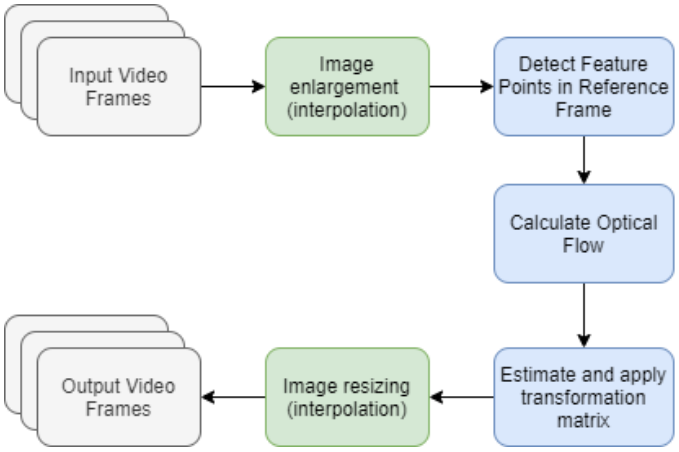


Figure 3.1: Video registration method.

#### 3.1.2.1 Feature Points Detector

The first step of a Point Feature Matching approach is to detect feature points that usually represent edges or corners of a given image (in the context, represent the microgroove wall and several agglomerates of non-motile cargoes spread all over the axon). A broad set of robust corner detector algorithms are already documented and universally used in image registration and object recognition.

The well-known Harris Corner Detector [66], developed in 1988, is one of the first attempts to find these feature points on an image. Therefore, *Harris and Stephens* [66] defined corner points as the ones with large intensity variation in all directions. Considering each pixel location as $(u,v)$ and its intensity as $I_{u,v}$, they defined the difference in intensity for a displacement window of $(x,y)$ as:

$$E_{(x,y)} = \sum_{u,v} w_{u,v}[I_{x+u,y+v} - I_{u,v}]^2 \tag{3.1}$$

For a corner, the difference between shifted intensity ($I_{x+u,y+v}$) and the original intensity ($I_{x,y}$) is very high. Therefore, the algorithm maximizes the second term of the above function using Taylor series expansion, obtaining the bellow final expression:

$$E_{(x,y)} = (x,y)M(x,y)^T \tag{3.2}$$

where the 2x2 symmetric matrix M is:

$$M = \begin{bmatrix} X^2 & XY \\ XY & Y^2 \end{bmatrix} \otimes w_{u,v} \tag{3.3}$$

and $X$, $Y$ are the first gradients in x and y directions, respectively.

Finally, to determine whenever a window contains a corner or not, a scoring function (Eq. 3.4) was defined using the eigenvalues of the symmetric matrix M ($\alpha$ and $\beta$). Therefore, null values of R are commonly related to flat regions, negative R values are related to edges and finally, high R values happens when the region is a corner.

$$R = \alpha\beta - k(\alpha+\beta)^2 = Det(M) - kTr(M)^2 \tag{3.4}$$

Some years later, *Shi and Tomasi* [67] developed an algorithm, which made a slight modification on the Harris Corner Detector scoring function (Eq. 3.5). This new approach turns to show better results than the original scoring function while reduces the computational effort.

$$R = min(\alpha,\beta) \tag{3.5}$$

For corner detection in the axonal transport videos, a function (which integrates the Shi-Tomasi Corner Detector algorithm) from OpenCV (Open Computer Vision Library) was used to find the four hundred stronger corners of the first frame which will be used as a reference to stabilize the image sequence.

#### 3.1.2.2 Optical Flow

To stabilize the video scene, once the feature points are found in the reference frame, it is necessary to track these points on each of the following frames and then calculate the apparent motion caused by the camera movement. Under certain assumptions, this projection called commonly as Optical flow, implement a good approximation of the overall motion [68].

The most fundamental assumption while estimate optical flow is intensity invariance between frames. Therefore, the relation between feature points in a sequence results in the Equation 3.6,

where $I(x,y,t)$ is the pixel intensity in the reference frame and $(dx,dy)$ is the motion captured in next frame taken after $dt$ time.

$$I(x,y,t) = I(x+dx,y+dy,t+dt) \tag{3.6}$$

To resolve the above Equation a first-order Taylor series approximation is taken to remove common terms and obtain the Optical Flow mathematical statement present in equation 3.7 (where $\frac{\partial I}{\partial x}$, $\frac{\partial I}{\partial y}$, and $\frac{\partial I}{\partial t}$ are the gradients along the horizontal axis, the vertical axis, and time). Therefore, the optical flow problem is to find $u$ and $v$ and determine movement over time. Against the unworkability to solve an Equation with two unknown variables, several methods over the years were developed to resolve the Optical Flow issue.

$$\begin{aligned} & \frac{\partial I}{\partial x}\partial x + \frac{\partial I}{\partial y}\partial y + \frac{\partial I}{\partial t}\partial t &&= 0 \\ \Leftrightarrow \quad & \frac{\partial I}{\partial x}\frac{\partial x}{\partial t} + \frac{\partial I}{\partial y}\frac{\partial y}{\partial t} + \frac{\partial I}{\partial t} &&= 0 \\ \Leftrightarrow \quad & u\frac{\partial I}{\partial x} + v\frac{\partial I}{\partial y} + \frac{\partial I}{\partial t} &&= 0 \end{aligned} \tag{3.7}$$

*Lucas and Kanade* ([69] proposed a robust technique to estimate the optical flow assuming high temporal resolution with small-time increment between consecutive frames and consequently slow-moving structures. Moreover, this method assumes that all the neighboring pixels around a feature point will have similar motion. Therefore, the Lucas-Kanade approach considers a small 3x3 window around a feature point and assumes that all neighborhood have the same motion, solving the basic optical flow Equation for all nine pixels. Thus, it is achieved a matrix with nine equations and two unknowns that are resolved with the least-squares criterion [70].

For optical flow detection in the axonal transport videos, the OpenCV library function, which integrates the Lucas-Kanade method, was used with the feature corners selected in the reference frame to find these same corners in a subsequent frame. As mentioned below, the Lucas-Kanade method only works for slow-moving structures. Nevertheless, the OpenCV implementation applies a pyramidal approach, where small motions are interactively ignored, and large motions are reduced to small ones [71].

#### 3.1.2.3 Transformation Matrix and output video

At this time, it is already known the location of the feature points in the reference and target frame. These two sets of points will be used to find the euclidean transformation matrix (Eq. 3.8) using a RANSAC based robust method. Therefore, this 2x3 matrix integrates the optimal

combination of translation ($t_x$ and $t_y$), rotation ($\theta$) and uniform scaling ($s$) to estimate the motion between frames.

$$M = \begin{bmatrix} \cos(\theta)s & -\sin(\theta)s & t_x \\ \sin(\theta)s & \cos(\theta)s & t_y \end{bmatrix} \tag{3.8}$$

For the described experimental setup, it is not expected a camera motion that allows the field of view rotation or scaling, resulting in a simplified transformation matrix where $\theta = 0$ and $s = 1$ (Eq. 3.9).

$$M = \begin{bmatrix} 1 & 0 & t_x \\ 0 & 1 & t_y \end{bmatrix} \tag{3.9}$$

Hereupon, the transformation matrix was estimated and applied for all video frames, and the stable output video was saved for further analysis.

#### 3.1.2.4 Evaluation

The overall stability improvement of the processed videos was evaluated comparing the global mean of each video sequence before and after registration. Results obtained for one representative video are compared in Figure 3.2, where Figure 3.2a depict the first video frame, Figure 3.2b depicts the mean of the original unprocessed sequence and Figure 3.2c presents the mean of the stabilized video. The algorithm efficiency is pointed out by the much smaller distortion of the output sequence and its similarity to the reference frame.

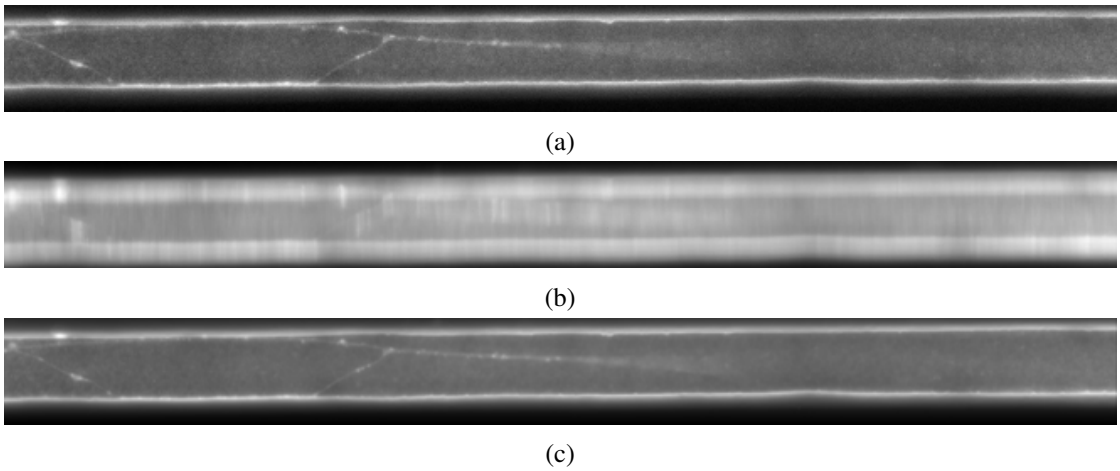

(a)

(b)

(c)

Figure 3.2: Video registration evaluation: (a) First video frame. (b) Mean of unprocessed video. (c) Mean of stabilized video.

### 3.1.3 Kymographs Acquisition

The microgrooves videos are hereupon stable and ready to be analyzed. It is already stated that tracking cargoes is a crucial task to extract quantitative information about axonal transport dynamics. Therefore, the stable time-lapse images from the axon will be analyzed with computer-vision techniques to recognize and follow cargoes across space and time. Although the recordings were taken with a high temporal resolution (5 $frames/s$), the spatial resolution is substantially smaller (pixel size range between 0.36 and 0.55 $\mu m$). Consequently, each imaged cargo within the axon has a diameter lower than 3 pixels leading to several segmentation problems while performing a truthful automatic cargo tracking over time. Alternatively, this thesis work relies on kymograph analyses to extract the required axonal transport kinematic parameters.

As stated in Section 2.4, there are already several software tools that compute kymographs from time-lapse recordings. One of these tools is *KymoResliceWide* [72], an open-source ImageJ plugin that generates kymographs from time-lapse videos, using different ROI types (straight line, polyline or freehand selection of variable thickness) to define the axon, and performing average or maximum intensity across the ROI. In this thesis work, the axon was defined as a polyline with variable thickness (3 pixels for 0.55 pixel size recordings, and 5 pixels for 0.36 pixel size recordings). The kymographs were computed with the maximum intensity across the line.

For kymograph generation, it is important to state that each video (or microgroove) has one to three axons, that were individually analyzed (one kymograph generate for each axon). All microgrooves were recorded with the cell body compartment on the top and the axonal compartment on the bottom. Therefore the axon grows up from top to bottom, and kymographs were acquired in the same direction.

Hereafter, it is necessary to define the cargoes trajectories on the kymograph. The overall research work on the area reports the general dissemination of trajectory manual assignment. Considering the subjectiveness and the dependency on user background to manually assign cargoes trajectories, this thesis presents a kymograph automatic segmentation and kinematic parameters extraction, following the method described in the next section.

### 3.1.4 Kymographs Segmentation

First of all, all kymographs generated were cropped to contain only one trajectory per kymograph, as shown in Figure 3.3a. A broad set of the acquired kymographs have several vertical stripes artifacts noticeable, caused by agglomerates of non-motile mitochondria, that are spread all over the axon. Moreover, there are also some shaded horizontal artifacts caused by differences in the light over the recording.

The regular orientation of the artifacts allows its significant reduction via frequency domain filtering. Therefore, the kymograph's Fast Fourier Transform (FFT) was computed, and the resultant magnitude spectrum is depicted in Figure 3.3b. In the spatial frequency domain, vertical stripes include high-frequency parts in the horizontal direction and the other way around [73].

Therefore, an adaptive mask (Fig.3.3c) on these region filtered out the stripes and result on the final restored image (after the Inverse Fast Fourier Transform (IFFT)) depicted in Figure 3.3d.

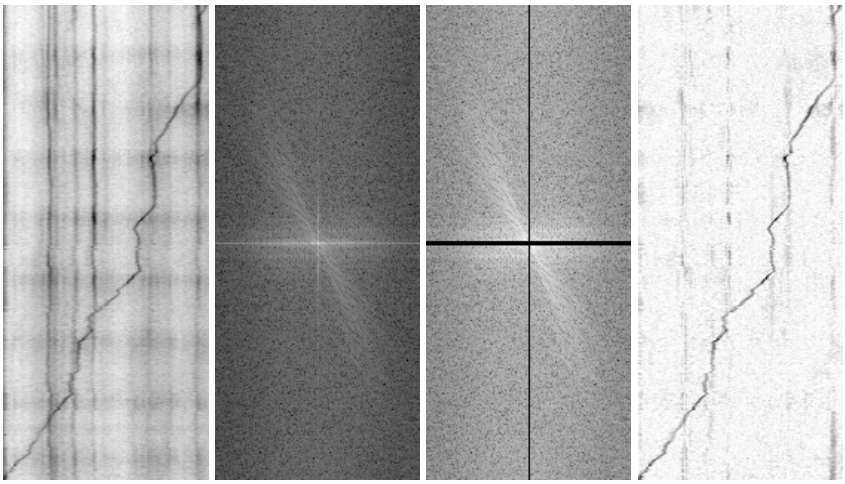

(a) (b) (c) (d)

Figure 3.3: Original representative kymograph (a) and its FFT magnitude spectrum before (b) and after (c) mask. Image (d) represents the post-processed kymograph.

In a nutshell, the segmentation algorithm adopted hereupon is composed of two different cycles. The first one uses the FFT transformed image and define an ROI to look for a trajectory. The second one applies the ROI to the FFT transformed image, and with refined parameters, establish the cargo trajectory. The described method is summed up in Figure 3.4.

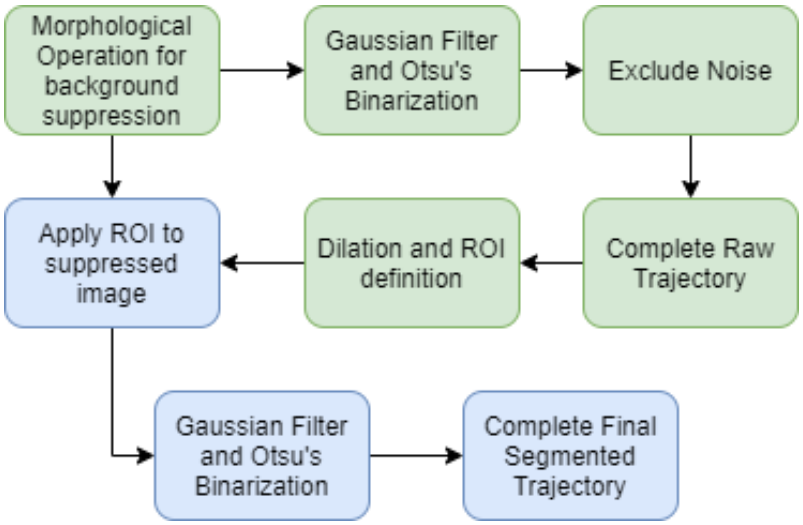


Figure 3.4: Trajectory segmentation method: first (green) and second (blue) cycle.

The first cycle begins to perform a background suppression using the grayscale Morphological Operation Opening on the FFT transformed image (Fig. 3.5a). Considering a kernel size slightly bigger than the trajectory thickness, these edges are blurred, and the resultant background image is subtracted to the original one (Fig. 3.5b). Then, it is applied an equally sized Gaussian Filter followed by an automatic Otsu's Binarization. The 2-D Gaussian Filter is a convolution operator used to blur the kymograph image, removing background noise. It is similar to the mean filter but uses a specific kernel that represents the shape of a Gaussian ('bell-shaped') curve.

As depicted in Figure 3.5c, the resultant image is still very noisy. Therefore, a set of operations are taken to maintain only the pixels that probably belong to the trajectory. The image is analyzed line by line, as an array, and the white pixels are allocated to a two-dimensional list. On the image, it was retained only the consecutive white pixels and the ones which belong to a search area, defined by the maximum velocity that cargo could achieve. The considered maximum absolute velocity was initially taken as 0.8 $\mu m/s$ (as report on the literature review). For trial and error, we find out that the cargoes seem to reach velocities up to the reported range, and then the search area was increased until achieving the result present in Figure 3.5d. The pointed high cargo velocity will be focused and better explored in the next section.

It was necessary to complete the non-segmented sections on the raw trajectory by drawing straight lines between non-consecutive pixels (Fig. 3.5e). Despite the already acceptable result, some information was lost on the process. Therefore, this first segmentation result was dilated to create a limited Region of Interest (Fig. 3.6a) to look for a refined trajectory.

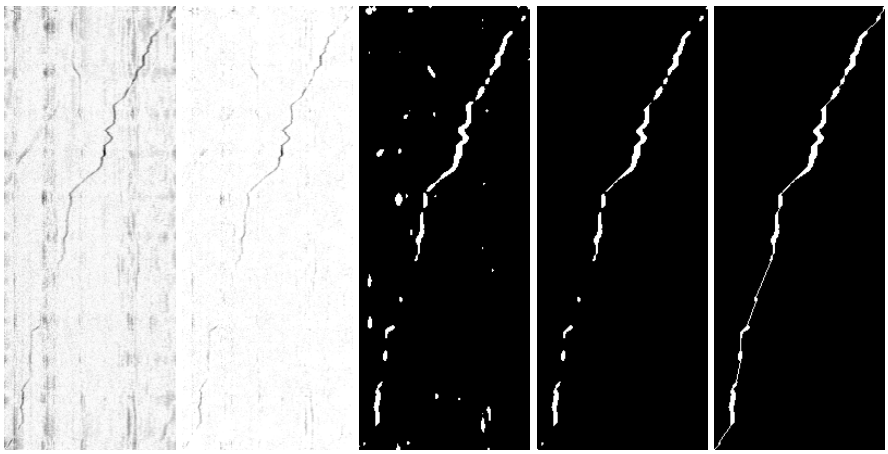

(a) (b) (c) (d) (e)

Figure 3.5: Kymograph segmentation evolution over first cycle: FFT transformation (a), background suppression (b), otsu's binarization (c), Noise Exclusion (d) and Raw trajectory (e).

The second cycle begins to apply the ROI mask to the background suppressed image (Fig.3.6b). Then, it is applied a trajectory thickness sized Gaussian Filter, followed by an automatic Otsu's Binarization (Fig.3.6c). One more time, the achieved trajectory was completed to close no segmented sections. Finally, the ultimate trajectory was depicted in Figure 3.6d.

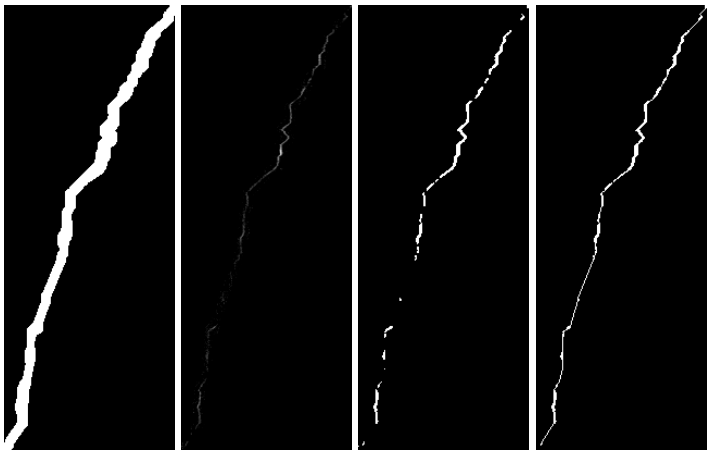

(a) (b) (c) (d)

Figure 3.6: Kymograph segmentation evolution over first cycle: dilated ROI (a), masked background suppressed image (b), otsu's binarization (c) and final trajectory (e).

### 3.1.5 Trajectory Linear Regression

After kymograph segmentation, it was necessary to find the exact cargo trajectory, composed by a variable number of linear regressions. To full fill this purpose, it was developed a methodology that runs the segmented trajectory, and iteratively finds the linear regression function that better describe a line segment. New pixels are included in the same line until the R-squared parameter (that determines how well the model fits the data) be optimized. The segmented lines were set to have at least 5 pixels, to avoid short meaningless trajectories sections. The instantaneous velocity was set as the linear regression slope and the mitochondrial time and position are saved to further kinematic parameters extraction. Figure 3.7 depicts a representative pre-processed kymograph and its final trajectory overlapped.

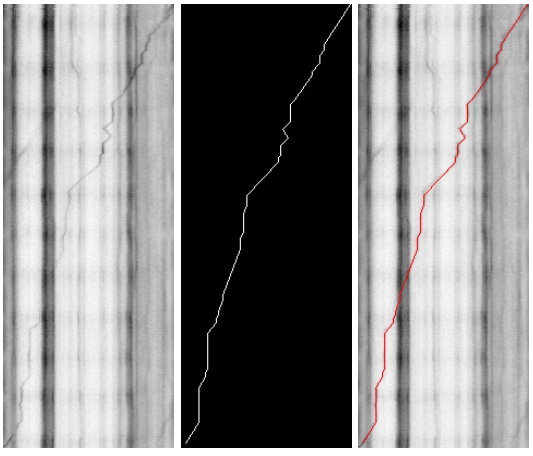

(a) (b) (c)

Figure 3.7: Kymograph trajectory assignment: original pre-Processed kymograph (a), kymograph trajectory (b) and overlay trajectory on kymograph (c).

## 3.2 Results and Discussion

Concerning kymograph segmentation, it is important to refer that some of the explained methodologies and parameters have to be individually adapted to each kymograph. Even though the developed algorithm offers satisfactory results to the majority images analyzed (as shown in the last section), some segmented trajectories do not reflect the true cargo run over time and space. Figure 3.7 depicts some examples of kymographs with resultant segmented trajectories.

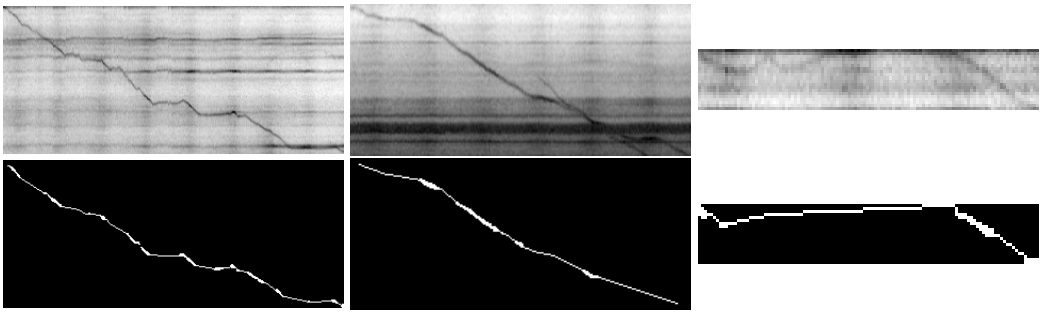

Figure 3.8: Original Kymographs (Top) and Segmented Trajectory (Bottom): from the left to the right it shows the decreasing on the segmentation capacity while the image quality decreases.

For further estimation of kinematic parameters and analysis of axonal transport dynamics, some unsuitable automatic trajectories were manually assigned using ImageJ.

### 3.2.1 Kinematics Parameters

Axonal transport is effectively characterized by its complex behavior and processes. Therefore, after fitting the segmented kymograph to a set of linear regression functions, the most reliable parameters to describe axonal transport dynamics were estimated, according to the literature review present in 2.2.

First of all, it is crucial to evaluate the cargo direction tendency. Figure 3.9a shows the overall direction distribution. Asymmetrically to the current research on the area, the overall favored direction is the retrograde one. This antagonist behavior reinforces the complexity behind axonal transport dynamics and its stability processes, emphasizing the necessity to deepen the research in the area with a wide collection of axonal transport video recordings.

Moreover, the same mitochondria seems to present different movement behavior over the run. Figure 3.9b depicts the percentage that the overall cargoes spent on each movement type. For this analysis, it is important to state that cargoes are considered static if its absolute velocity is slower than 0.05 $\mu m/s$ and pausing if its absolute velocity is between 0.05 and 0.12 $\mu m/s$.

Therefore, both high bidirectional mitochondria percentage and combined prevalence of static and pausing cargoes, seem to support the "stop-and-go" hypothesis of axonal transport. As a matter of fact, on the recording data, bidirectional fast movements are mostly interleaved with pausing or even static moments.

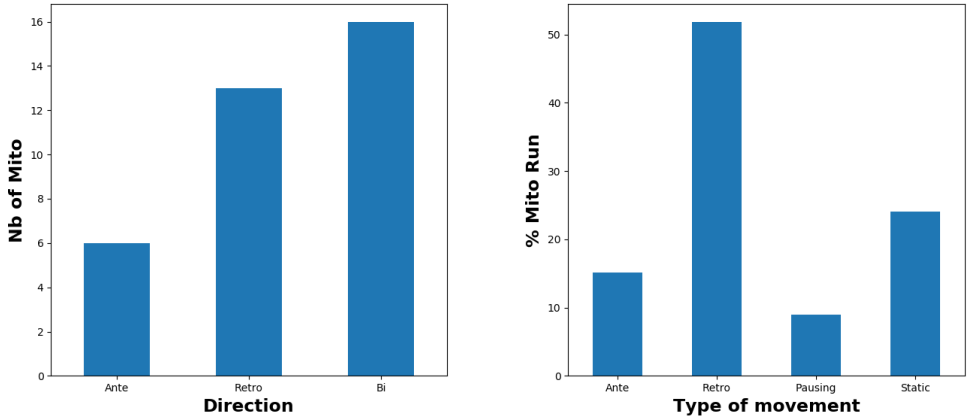


(a) (b)

Figure 3.9: Mitochondrial trafficking evaluation: (a) Directionality. (b) Movement behavior.

Concerning the cargo run length distribution and according to Figure 3.10, almost 60% of the cargoes have short runs (with less than 20 $\mu m$). It is crucial to state that some of the short runs are indeed longer, but at some time on the record, they disappear from the microscope focal plane. Therefore, it is reasonable to think that some of these mitochondria are indeed portions of a longer unique run. Additionally, it is visible that 60% of the longer runs (with more than 20 $\mu m$) are bidirectional. Once again, this tendency reinforces the mitochondrial complex behavior and the underlying regulatory mechanisms which support the turnovers, to ensure axon (and neuron) structure and function.

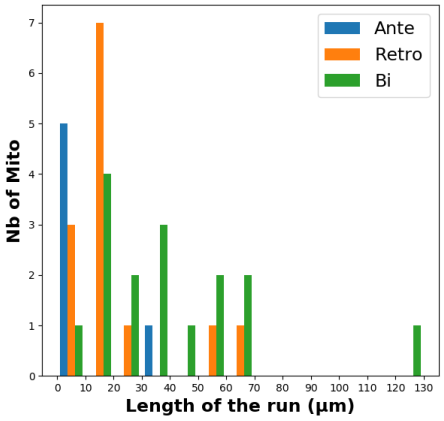


Figure 3.10: Mitochondrial run length distribution.

The most used and reliable kinematic parameter to assess axonal transport dynamics is cargo velocity. Therefore, Figure 3.11 shows both instantaneous (Fig.3.11a) and mean (Fig.3.11b) velocity distribution for the given recorded data. Instantaneous velocity is set as the slope of the kymograph optimized linear regression functions.

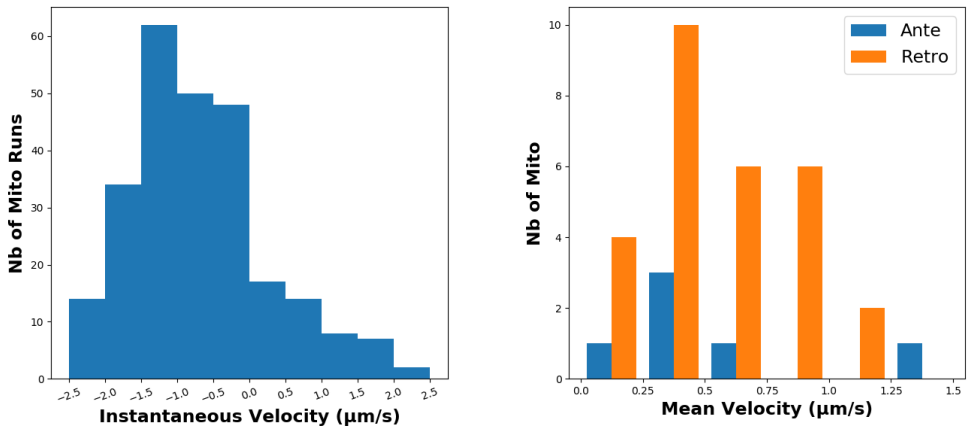


(a) (b)

Figure 3.11: Mitochondrial velocity evaluation: instantaneous (a) and mean (b) velocity distribution.

The current work on the area reports the normal instantaneous range velocity of mitochondrial movement as slower than 0.8 $\mu m/s$ (for both anterograde and retrograde direction). Figure 3.11a depicts that only 41% of the cargoes have instantaneous velocity in between the mentioned range. In fact, the analyzed data express a wide range of values, including instantaneous velocities up to 2.0 $\mu m/s$ (for both anterograde and retrograde transport). Concerning mean velocities, the distribution seems to be more aligned with the reported literature with more than 75% of the mitochondria within the range. To understand better this abnormal behavior, Figure 3.12a and 3.12b shows, respectively, the distribution of the moving time and run length with the instantaneous velocity range.

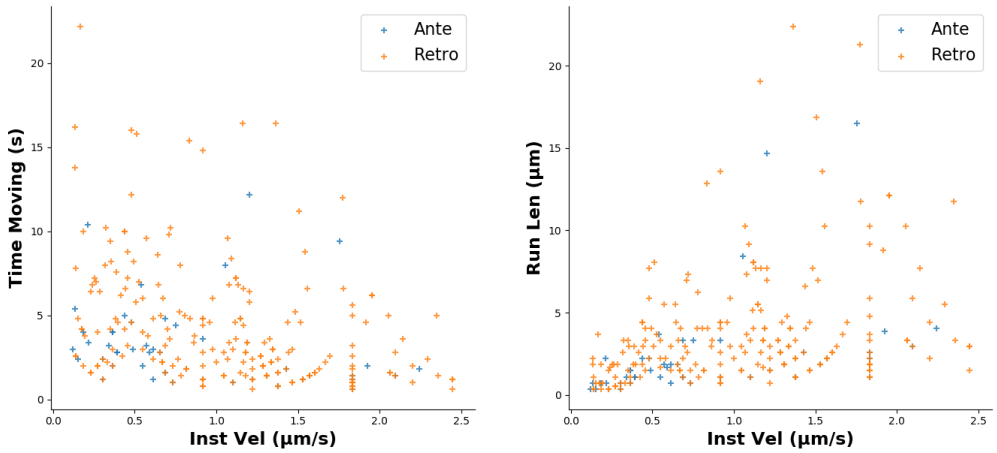


(a) (b)

Figure 3.12: Instantaneous velocity correlation with time moving (a) and run length (b).

It is clear that cargoes with high velocity (up to 2 $\mu m/s$) are moving for short periods (less than 5 seconds). Otherwise, the run-length distribution over the velocity range seems to be more equitable, with no obvious tendency for cargoes with high velocity.

Therefore, to validate the authenticity of these results, we perform a manual fitting to a kymograph trajectory with multiple sections with high instantaneous velocity. The results are present in Figure 3.13 and Table 3.1.


Figure 3.13: Kymograph trajectory

Table 3.1: Kymograph trajectory raw coordinates - final ($X_f$, $Y_f$) and initial ($X_i$,$Y_i$), and resultant instantaneous velocity calculated from A to E. The analyzed video were recorded at 5 Hz and the pixel size is 0.3667 $\mu m$.

| | $\mathbf{X_i}$ | $\mathbf{Y_i}$ | $\mathbf{X_f}$ | $\mathbf{Y_f}$ | $\mathbf{V_{inst}}$ $(\mu m/s)$ |
|---|---|---|---|---|---|
| A | 150 | 792 | 141 | 800 | -2.06 |
| B | 141 | 803 | 132 | 811 | -2.06 |
| C | 129 | 824 | 125 | 827 | -2.44 |
| D | 98 | 890 | 90 | 896 | -2.44 |
| E | 90 | 896 | 97 | 903 | 1.83 |

The manual assignment of the kymograph trajectory confirms the existence of high velocity run sections, and discard a possible systematic error on automatic segmentation or linear regression.

### 3.2.2 Graphical User Interface

The methodology described in the last sections runs in Python and it is available through a self-made graphical user interface (KymoView), developed using Tkinter library. KymoView provides easy, dynamic, and effective access to the kymograph segmentation results, and kinematic graphical visualization and exportation.

Figure 3.14 shows the main windows of the KymoView interface. The user could upload several kymographs and respective acquisition parameters. Therefore each segmented kymograph could be visualized, and the graphical analysis of the kinematic parameters accessed and extracted. If the provided kymograph segmentation was unsuitable, the user could set a manual trajectory. Raw kinematic data could also be compiled and exported to *.xls* file. The current workspace with kymograph analysis could be saved to *.npy* file to allow the entire interface to be loaded later with the exported data.

KymoView complete description and user manual are present in Appendix A.

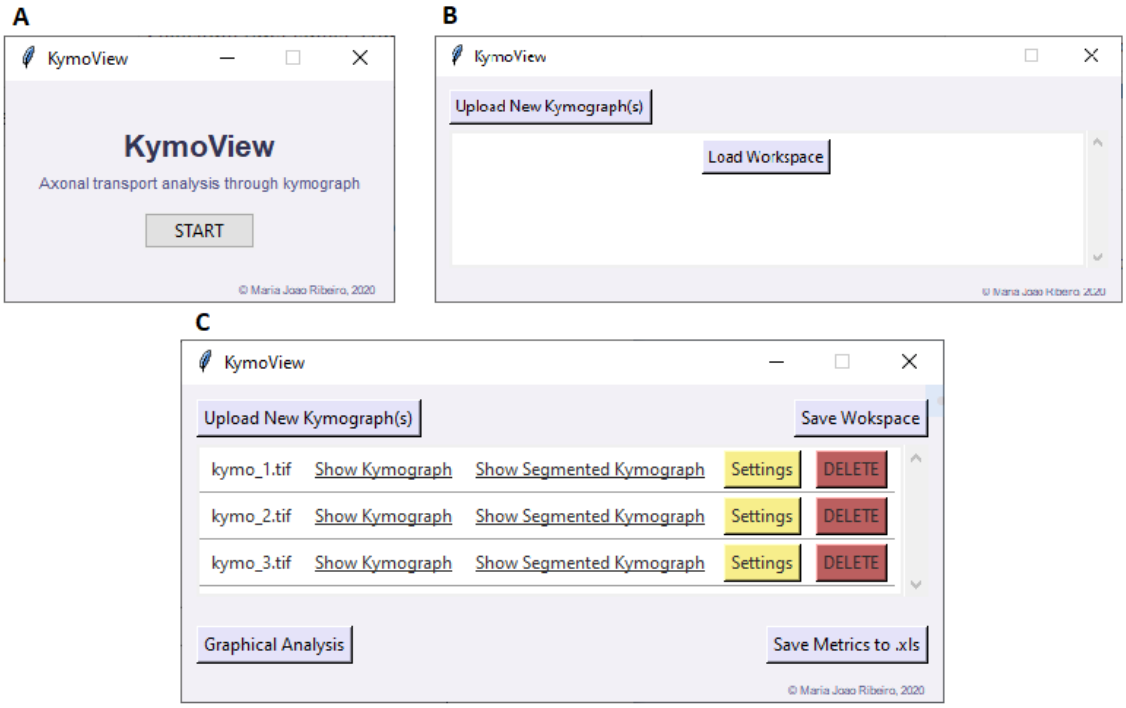


Figure 3.14: KymoView GUI: first window (A), main window empty (B) and with a workspace loaded (C)

# Chapter 4

# Electrophysiological Recordings Analysis

Despite its utmost importance, the principles behind the relationship between axonal transport dynamics and correspondent activity and maturation stage of the neuronal network remain unclear. As stated in chapter 2, this simultaneous evaluation is allowed using a combined platform of MEAs and microfluidics chamber, to capture videos of axonal transport in individualized axon and simultaneously record the APs propagation along the same axon. Therefore, the present chapter introduces a methodological procedure to import, visualize, and analyze electrophysiological recordings in order to evaluate the activity of a given axon within a microgroove. This will aid in further scrutinizing the relationship between neuronal activity and axonal transport dynamics.

## 4.1 Methods

The entire procedure was developed and tested with electrophysiological data recorded for previous work in the Neuroengineering and Computational Neuroscience Research Group. The data comprises the spontaneous activity of embryonic rat DRG explant cultures on $\mu$EFs, at DIV 7.

### 4.1.1 Experimental Setup

#### 4.1.1.1 $\mu$EF platform preparation

$\mu$EF platforms were prepared by placing the microfluidic devices against a pre-coated MEA (Multichannel Systems) with 256 electrodes (30 $\mu$m in diameter and interspaced of 100 $\mu$m), as described elsewhere [9]. In brief, the MEAs were coated with 0.01 mg/ml of poly(D-lysine) (PDL, Corning), overnight at 37 °C. Microfluidic devices were sterilized with 70% ethanol and were gently attached to the PDL-coated MEAs/ coverslips, creating a $\mu$EF/ microfluidic chamber composed of two separate cell seeding compartments connected by microgrooves. The cell

seeding compartments were then loaded 5 $\mu$g/ml laminin isolated from mouse Engelbreth-Holm-Swarm sarcoma (Sigma-Aldrich Co.) and incubated overnight at 37 °C. The unbound laminin-1 was removed, and the chambers were refilled with culture medium and left to equilibrate for at least 2 h at 37 °C prior to cell seeding.

#### 4.1.1.2 DRG explant culture

Experimental procedures involving animals were carried out in accordance with current Portuguese laws on Animal Care (DL 113/2013) and with the European Union Directive (2010/63/EU) on the protection of animals used for experimental and other scientific purposes. The experimental protocol (reference 0421/000/000/2017) was approved by the ethics committee of the Portuguese official authority on animal welfare and experimentation (Direção-Geral de Alimentação e Veterinária). All possible efforts were made to minimize the number of animals and their suffering. Unless otherwise stated, all reagents listed below are from Gibco, Thermo Fisher Scientific. DRG explants were obtained as described in Chapter 3. For each $\mu$EF platform, one DRG explant was seeded in the cell body compartment and cultured in a humidified incubator at 37 °C supplied with 5% $CO_2$.

### 4.1.2 Electrophysiological recording

The spontaneous activity of DRG explant cultures was recorded at DIV 7, using a MEA2100 recording system (Multichannel Systems MCS GmbH, Germany) (see section 2.3 for details). Extracellular recordings were obtained at a sampling rate of 50 kHz over 1 minute. Raw data files were exported to HDF5 (Hierarchical Data Format 5) files using the Multichannel Data Manager, which facilitates the data analysis with a third-party program (in this thesis, the data was analyzed with Python programming language).

HDF5 is a data model and file format for storing and managing high volume and complex hierarchical data. An HDF5 file can be noticed as a container (group) that holds other containers or a variety of heterogeneous data objects (datasets). The datasets can be simple arrays or even images, tables, graphs, or documents. The metadata is stored in the form of user-defined attributes attached to groups and datasets. [74].

A MCS-HDF5 file contains one principal group that holds all recordings for an experiment. Each recording includes other different containers corresponding to different stream types. For this analysis, it was only used the group which contains all channel-based streams of the recordings. This group contains 3 different objects: *ChannelData* (voltage data recorded for all sampled electrodes), *ChannelDataTimeStamps* and *InfoChannel* (information about electrodes labels, conversion factors and physical units of the measured values). All the analysis using the above data were carried out using *McsPy* - a Python package that handle HDF5 raw data files, which were converted from recordings of Multi-Channel Systems devices [75].

## 4.2 Results and Discussion

Since the MEA chip and the microfluidic platform are aligned, it is necessary to visualize the data from all 252 electrodes (Figure 4.1) and recognize which electrodes are recording each microgroove.

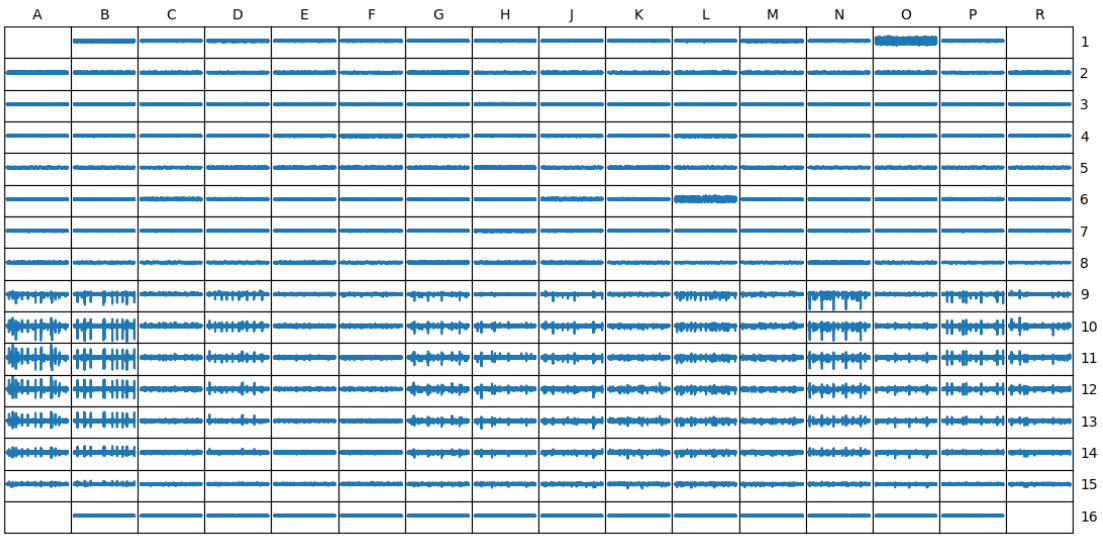


Figure 4.1: Signal read in each electrode sampled in Python for 5 seconds.

As shown in Figure 2.8b, each microgroove encloses 6 electrodes from a single MEAs column. According to Figure 4.1, there are 16 microgrooves analyzed in this experiment (columns A to R) with electrodes from lines 9 to 14, which leads to different active regions of interest that could be analyzed individually. The first 8 lines correspond to the cell body compartment (without microchannels). Collums without activity is the result of microgrooves without any axon (or electrically inactive axons).

Figure 4.2 depicts the recordings from a single microgroove, therefore the electrical activity is visualized in more detail and several spike events are discernible. Figure 4.2a shows the microgroove activity sampled over 30 seconds, while Figure 4.2b depicts a single spike propagation over the axon (i.e. AP displacement over time).

### 4.2.1 Spike Detection

For each channel, the signal was filtered with a fourth-order bandpass (300-6000 Hz) Butterworth filter [76]. With the filtered signal, the spikes were detected by amplitude thresholding with a minimum separation in between peaks of 2 ms. The threshold was automatically set as stated in equation 4.1, where $|M_n|$ is the median of the absolute filtered signal used to estimate the standard

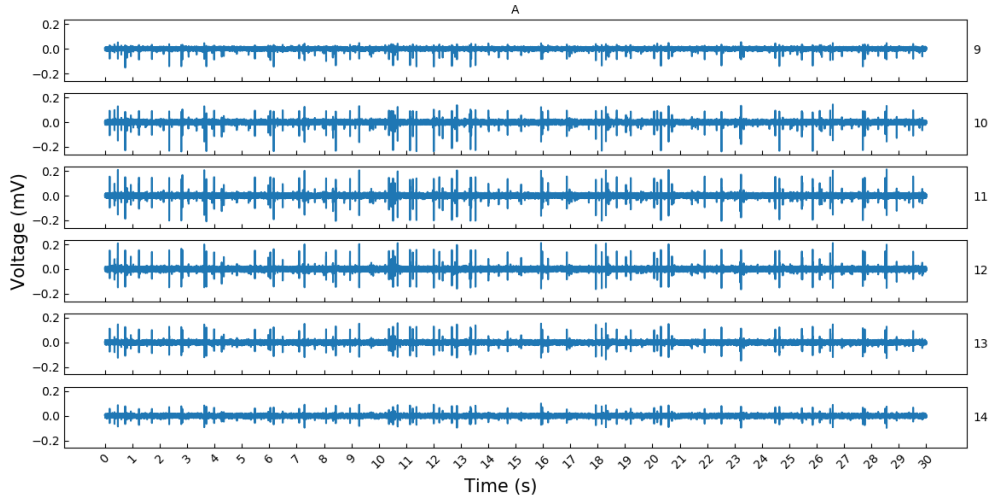


(a)

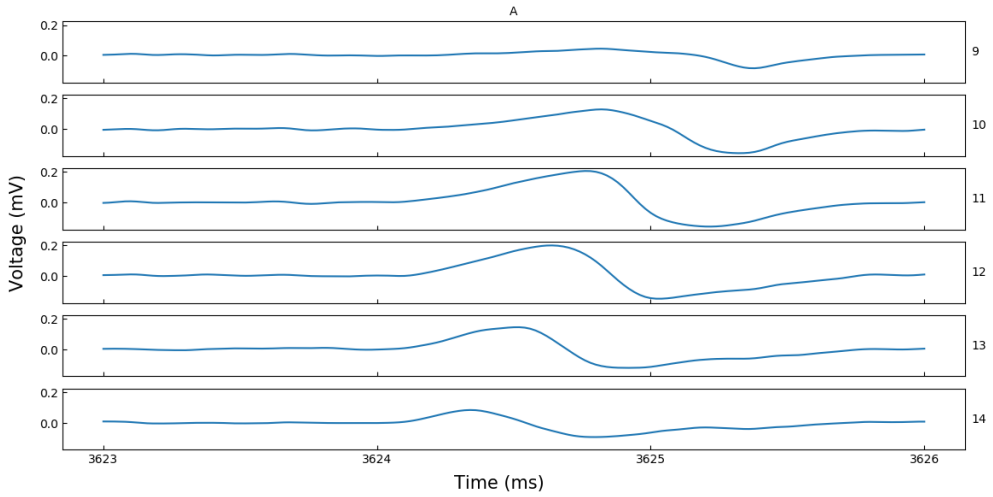


(b)

Figure 4.2: Signal read in a microgroove electrodes sampled in Python for 30 seconds(a) and a spike propagation (b).

deviation ($\sigma_n$) of the remaining data [50]. Therefore, the detection threshold was calculated as the number ($n_\sigma$) of standard deviations above or below the median.

$$Th = |M_n| + n_\sigma \sigma_n \Rightarrow n_\sigma = 4 \tag{4.1}$$

The raster plot resultant of the spike detection on the four central channels of the first microgroove is shown in Figure 4.3.

The electrophysiological activity of a neural network could also be analyzed using a representative (central) electrode within a microgroove. Therefore Figure 4.4a shows the electrical activity of a single channel with the detected spikes marked over five seconds.

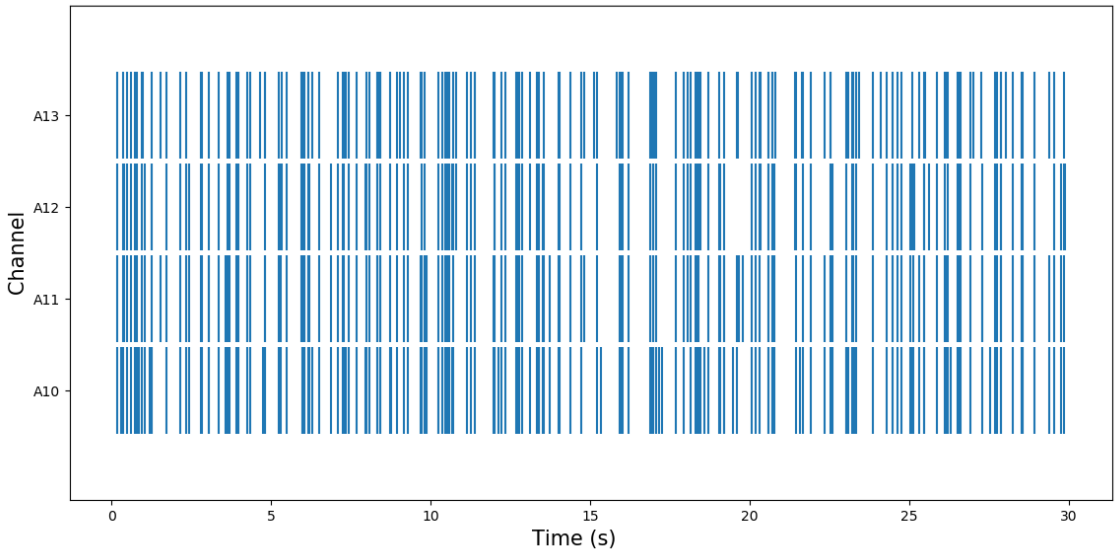


Figure 4.3: Raster plot of the spikes detected using the thresholding method in the first microgroove.

### 4.2.2 Firing Rate Analysis

To understand the relationship between electrophysiological activity and axonal transport dynamics, the global and instantaneous firing rates of each channel were calculated. Therefore, for further analysis, the evolution of the firing rate dynamics over time could be associated with particularly cargoes velocities or pausing times.

The firing rate is commonly defined as the number of spikes a neuron fires per unit of time. On the recordings analyzed, the maximum firing rate obtained for the total minute of recording was 10 Hz, which is a value compatible with the stated in the literature for the spontaneous activity of DRG neurons on DIV 7.

Additionally, for each channel, the instantaneous firing rate (IFR) was calculated by convolving the spike train with a Gaussian window with 100 ms. Figure 4.4b depicts the IFR evolution of the target channel over five seconds.

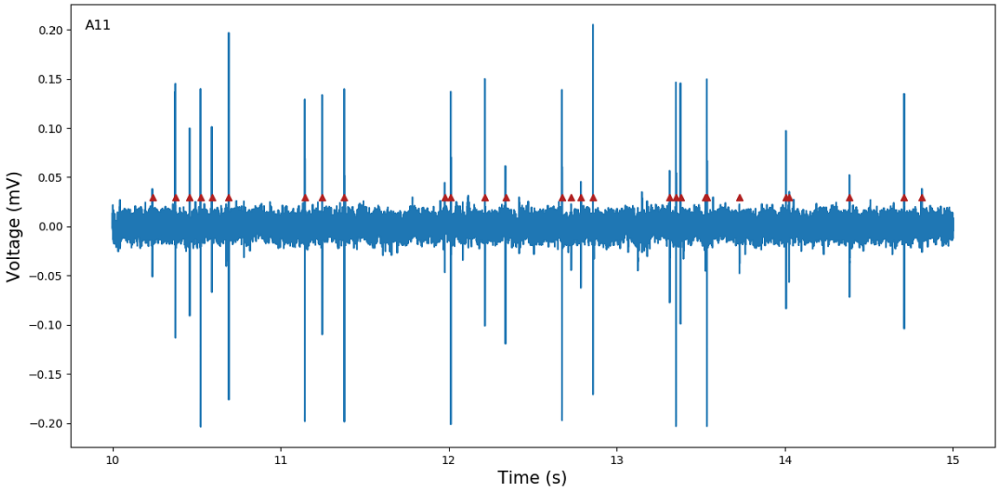


(a)

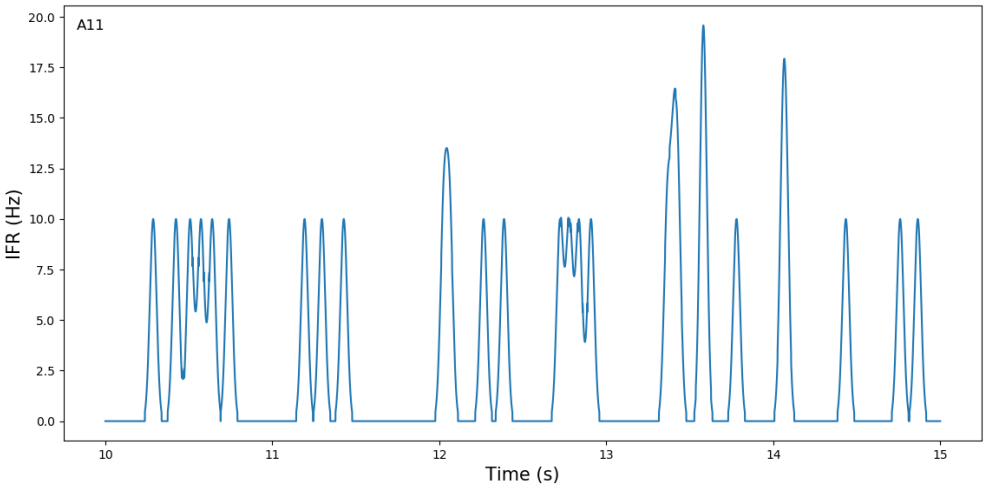


(b)

Figure 4.4: Signal read in a single electrode with spikes detected (a) and correspondent instantaneous firing rate (b).

# Chapter 5

# Conclusions

In human, PNS neurons could achieve over a meter long. Therefore, the efficient axonal communication and intracellular cargoes transportation turns to be crucial to its structure maintenance and carriage of electrical signals. Many neurodegenerative diseases are characterized by axonal transport defects and lead to progressive deterioration of the nervous system with a significant decrease in the patients' quality of life. To understand such complex behavior, many efforts have been taken to construct experimental and technological tools that aid to reveal the mechanisms controlling the axonal transport dynamics, and its relationship with the electrical activity and signal carriage through the neuronal network.

Therefore, this work focused on the development of computational tools to analyze axonal transport fluorescence microscopy videos and extract kinetics parameters to describe the axonal cargoes movement. Due to the lack of stability of the recording system installed on the microscope, it was imperative to perform a video registration, stabilizing all frames in the same coordinate system to allow the integration of the data obtained from the different frames. Although the video recordings were taken with a high temporal resolution, the spatial resolution is substantially smaller. Consequently, each imaged cargo within the axon has low diameter leading to several segmentation problems while performing a truthful automatic cargo tracking over time. Alternatively, this thesis work relies on kymograph analyses and its cargoes trajectory definition. Therefore it was developed an automatic kymograph segmentation method to allow kinematic parameters extraction.

Although the stable segmentation results on a representative quantity of data, the algorithm still presents limitations on the noisy kymographs segmentation and computational parameters generalization. The axonal transport dynamics were analyzed through visualization of direction tendency, movement and pausing behavior, run-length distribution, velocity distribution, and the relationship between these parameters. This analysis presents an antagonist behavior, which reinforces the complexity behind axonal transport dynamics and its stability processes. To achieve deeper conclusions, it will be necessary to broaden the analyzed dataset.

Furthermore, the developed tools provide a Graphical User Interface - KymoView - to efficient access to the segmentation and kinematic results.

Otherwise, this dissertation also describes a methodological procedure to import, visualize and analyze electrophysiological recordings in order to evaluate the activity (characterized through global and instantaneous firing rates) of a given axon within a microgroove. This will aid in further scrutinizing the relationship between neuronal activity and axonal transport dynamics.

Altogether, the developed tools are ready to be used to analyze the axonal transport dynamics and the electrophysiological network activity. Even though this work does not directly contribute to the scrutinization of the problem presented in the Introduction, it provides a set of tools that can be further combined to achieve this objective.

# Chapter 6

# Future Work

This dissertation provides computational tools for combined analysis of axonal transport dynamics and neuronal electrophysiological activity. However, during the course of this work, these tools were neither tested nor applied to data from the same experiment. Therefore, additional common data recordings should be taken to allow this parallel analysis and tools validation.

Concerning the developed segmentation algorithm, a broad set of data will be also favorable to optimize parameters or even try some Machine Learning Segmentation techniques that also require a huge set of labeled data.

Regarding electrophysiological recordings analysis, after establishing its combined use with the image analysis tools, it will be also advantageous to include an additional module on the Graphical User Interface that guide the user through the developed procedure and allows the simultaneous visualization and saving of correlated data (e.g. recordings from the same microgroove and period).

# Appendix A

# KymoView User Manual

KymoView is a computational tool that provides efficient and user-friendly access to axonal transport analysis through kymograph. This manual encompasses step-by-step instruction notes to runs KymoView and fully profit for its use.

The first window showed while runs the GUI is present in Figure A.1.A and then, the main window (Fig. A.1.B) is opened. On the main window, the user has the possibility to load *.npy* files, previously exported by KymoView, or upload new kymograph(s) to be analyzed.

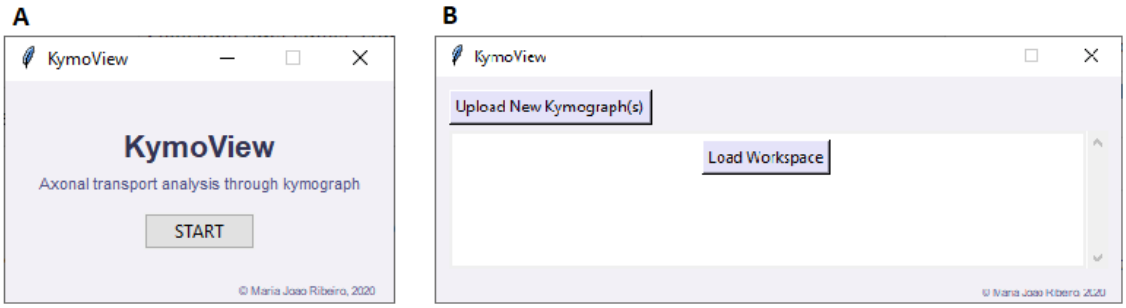


Figure A.1: First window (A) to open main menu window (B).

To upload new kymographs (Fig.A.2) a set of parameters must be provided:

- the video acquisition settings, such as frame rate and pixel size. The user must fill a valid number or rather the interface will return an error message.
- the segmentation preferences according to kymograph features, such as whether or not the kymograph(s) have vertical stripes to be suppressed and the background color.
- the kymographs(s) corresponding microgroove. The user has the possibility to add a new kymograph or choose between the existing ones.

After kymograph uploading, a progress window will (Fig.A.2.C) will pop up until the data finished to be analyzed.

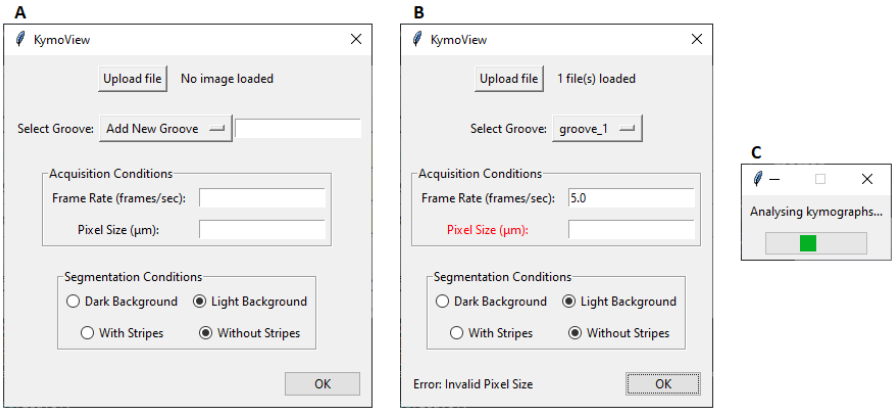


Figure A.2: Kymograph upload window (A), with microgroove selected and error message due to no pixel size entry (B) and progress window (C).

Hereupon, on the main window (Fig.A.3.A) the user accesses to the list of all already upload kymographs and has a set of features to explore related to them. First of all, the user could depict both original (Fig.A.3.B) and segmented (Fig.A.3.C) kymograph to verify whether or not the segmentation algorithm works properly. Additionally, the user could delete any kymograph from the workspace and save the current workspace to a *.npy* file to load later.

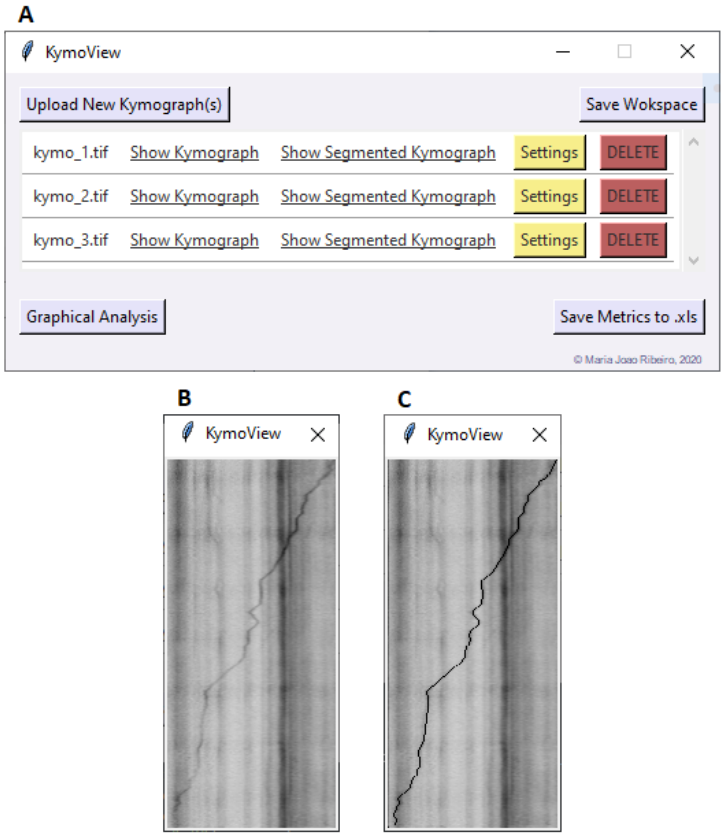


Figure A.3: Main window with workspace load (A) that allows original (B) and segmented (C) kymograph visualization.

Beyond kymograph visualization, the user could change some settings (Fig.A.4.A), either concerning acquisition or segmentation. If the case that the provided kymograph segmentation is unsuitable, the user could also set a manual trajectory by mouse drag and drop to create lines (Fig.A.4.B).

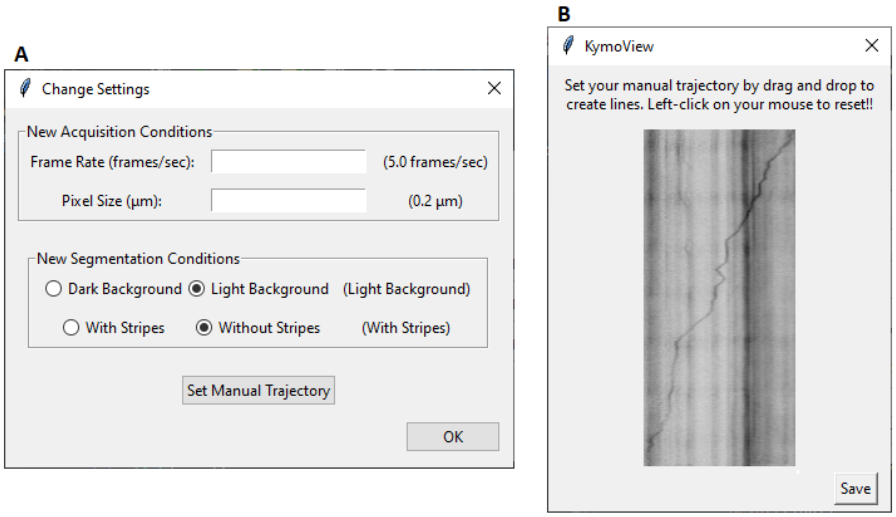


Figure A.4: Changing Settings Window (A) that also support Manual Trajectory Assignment (B)

The axonal transport dynamics exploration is provided depicting the graphical analysis described in 3.2.1 (Fig.A.5.A). Every graphic is available on an individual tab and could be saved to *.png* file to further considerations. Finally, trajectories and kinematic parameters could be export to *.xls* file organized by microgroove and properly identified (Fig.A.5.B).

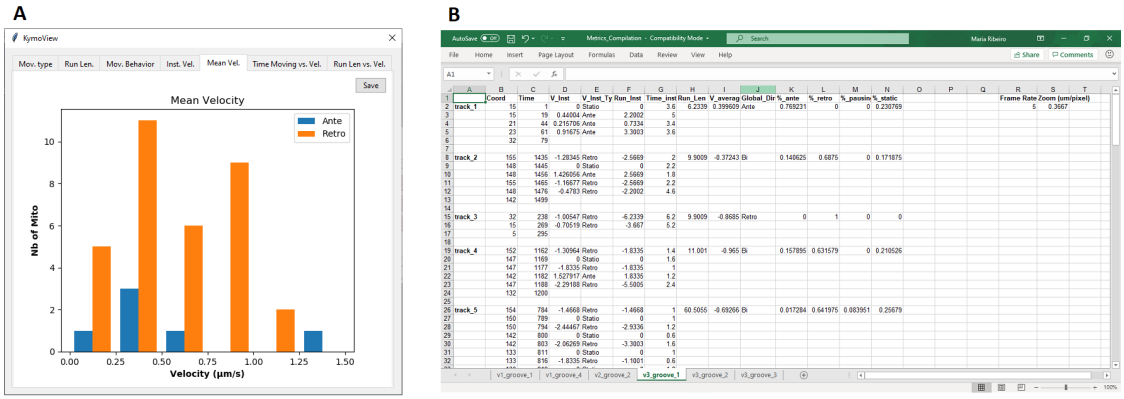


Figure A.5: Kinematic parameters graphical visualization (A) and resultant trajectory compilation saved to .xls file (B).

# References


[1] Anders Rehfeld, Malin Nylander, and Kirstine Karnov. Nerve tissue. In *Compendium of Histology: A Theoretical and Practical Guide*, pages 247–266. Springer International Publishing, Cham, 2017.

[2] David Sterratt, Bruce Graham, Andrew Gillies, and David Willshaw. *Principles of Computational Modelling in Neuroscience*. Cambridge University Press, 2011.

[3] Zu-Hang Sheng. Mitochondrial trafficking and anchoring in neurons: New insight and implications. *The Journal of Cell Biology*, 204(7):1087–1098, 2014.

[4] Jason E. Duncan and Lawrence S.B. Goldstein. The genetics of axonal transport and axonal transport disorders. *PLoS Genetics*, 2(9):1275–1284, 2006.

[5] P.C. Bridgman and M. Ahmed. Myosin Transport and Neuronal Function. In Larry R. Squire, editor, *Encyclopedia of Neuroscience*, pages 1187 – 1193. Academic Press, Oxford, 2009.

[6] Microelectrode array for USB-MEA256-System and MEA2100-HS256. https://www.multichannelsystems.com/products/microelectrode-arrays/256mea10030ir-ito. (Accessed on 01/11/2020).

[7] Wendy W. Liu, Joseph Goodhouse, Noo Li Jeon, and L. W. Enquist. A Microfluidic Chamber for Analysis of Neuron-to-Cell Spread and Axonal Transport of an Alpha-Herpesvirus. *PLOS ONE*, 3(6):1–10, 06 2008.

[8] Hyung Joon Kim, Jeong Won Park, Jae Byun, Wayne Poon, Carl Cotman, Charless Fowlkes, and Noo Jeon. Quantitative Analysis of Axonal Transport by Using Compartmentalized and Surface Micropatterned Culture of Neurons. *ACS Chemical Neuroscience*, 3:433–438, 06 2012.

[9] Cátia Lopes, José Mateus, and Paulo Aguiar. Interfacing Microfluidics with Microelectrode Arrays for Studying Neuronal Communication and Axonal Signal Propagation. *Journal of Visualized Experiments*, 12 2018.

[10] MEA2100-Systems. https://www.multichannelsystems.com/products/mea2100-systems#description. (Accessed on 01/15/2020).

[11] Amanda L. Neisch, Adam W. Avery, James B. Machamer, Min gang Li, and Thomas S. Hays. Chapter 14 - Methods to identify and analyze gene products involved in neuronal intracellular transport using Drosophila. In *The Neuronal Cytoskeleton, Motor Proteins, and Organelle Trafficking in the Axon*, volume 131 of *Methods in Cell Biology*, pages 277 – 309. Academic Press, 2016.

[12] Vladimír Ulman, Martin Maška, Klas E.G. Magnusson, Olaf Ronneberger, Carsten Haubold, Nathalie Harder, Pavel Matula, Petr Matula, David Svoboda, Miroslav Radojevic, Ihor Smal, Karl Rohr, Joakim Jaldén, Helen M. Blau, Oleh Dzyubachyk, Boudewijn Lelieveldt, Pengdong Xiao, Yuexiang Li, Siu Yeung Cho, Alexandre C. Dufour, Jean Christophe Olivo-Marin, Constantino C. Reyes-Aldasoro, Jose A. Solis-Lemus, Robert Bensch, Thomas Brox, Johannes Stegmaier, Ralf Mikut, Steffen Wolf, Fred A. Hamprecht, Tiago Esteves, Pedro Quelhas, Ömer Demirel, Lars Malmström, Florian Jug, Pavel Tomancak, Erik Meijering, Arrate Muñoz-Barrutia, Michal Kozubek, and Carlos Ortiz-De-Solorzano. An objective comparison of cell-tracking algorithms. *Nature Methods*, 14(12):1141–1152, 2017.

[13] Klas Magnusson, Joakim Jalden, Penney Gilbert, and Helen Blau. Global Linking of Cell Tracks Using the Viterbi Algorithm. *IEEE transactions on Medical Imaging*, 34, 11 2014.

[14] Anthony Brown. Axonal transport of membranous and nonmembranous cargoes : a unified perspective . *The Journal of Cell Biology*, 160(6):817–821, 03 2003.

[15] Stéphanie Millecamps and Jean Pierre Julien. Axonal transport deficits and neurodegenerative diseases. *Nature Reviews Neuroscience*, 14(3):161–176, 2013.

[16] Dominique Debanne, Emilie Campanac, Andrzej Bialowas, Edmond Carlier, and Gisèle Alcaraz. Axon physiology. *Physiological Reviews*, 91(2):555–602, 2011. PMID: 21527732.

[17] Kurt J. De Vos, Andrew J. Grierson, Steven Ackerley, and Christopher C.J. Miller. Role of Axonal Transport in Neurodegenerative Diseases. *Annual Review of Neuroscience*, 31(1):151–173, 2008. PMID: 18558852.

[18] Patrícia Batista and Anabela Pereira. Quality of Life in Patients with Neurodegenerative Diseases. *Journal Neurology and Neurosciences*, 7, 02 2016.

[19] Katharine Gammon. Neurodegenerative disease: Brain windfall. *Nature*, 515:299–300, 11 2014.

[20] Kazuki Obashi and Shigeo Okabe. Regulation of mitochondrial dynamics and distribution by synapse position and neuronal activity in the axon. *The European journal of neuroscience*, 38, 2013.

[21] Chuan Li Zhang, P L Ho, Douglas B. Kintner, Dandan Sun, and Shing Yan Chiu. Activity-dependent regulation of mitochondrial motility by calcium and Na/K-ATPase at nodes of Ranvier of myelinated nerves. *The Journal of neuroscience : the official journal of the Society for Neuroscience*, pages 3555–66, 2010.

[22] Marija Sajic, Vincenzo Mastrolia, Chao Yu Lee, Diogo Trigo, Mona Sadeghian, Angelina J. Mosley, Norman A. Gregson, Michael R. Duchen, and Kenneth J. Smith. Impulse Conduction Increases Mitochondrial Transport in Adult Mammalian Peripheral Nerves In Vivo. *PLoS Biology*, 11(12):e1001754, 2013.

[23] Eve Moutaux, Wilhelm Christaller, Chiara Scaramuzzino, Aurélie Genoux, Benoit Charlot, Maxim Cazorla, and Frédéric Saudou. Neuronal network maturation differently affects secretory vesicles and mitochondria transport in axons. *Scientific Reports*, 8, 12 2018.

[24] Nobuhiko Ohno, Grahame J. Kidd, Don Mahad, Sumiko Kiryu-Seo, Amir Avishai, Hitoshi Komuro, and Bruce D. Trapp. Myelination and Axonal Electrical Activity Modulate the Distribution and Motility of Mitochondria at CNS Nodes of Ranvier. *Journal of Neuroscience*, 31(20):7249–7258, 2011.

[25] Sotaro Ichinose, Tadayuki Ogawa, and Nobutaka Hirokawa. Mechanism of Activity-Dependent Cargo Loading via the Phosphorylation of KIF3A by PKA and CaMKIIa. *Neuron*, 87(5):1022 – 1035, 2015.

[26] J. de Wit, R.F.G. Toonen, J. Verhaagen, and M. Verhage. Vesicular trafficking of semaphorin 3A is activity-dependent and differs between axons and dendrites. *Traffic*, 7(8):1060–1077, 2006.

[27] Gordon Rintoul, Anthony Filiano, Jacques Brocard, Geraldine Kress, and Ian Reynolds. Glutamate Decreases Mitochondrial Size and Movement in Primary Forebrain Neurons. *The Journal of neuroscience : the official journal of the Society for Neuroscience*, 23:7881–8, 09 2003.

[28] Diane T. W. Chang, Anthony S. Honick, and Ian J. Reynolds. Mitochondrial Trafficking to Synapses in Cultured Primary Cortical Neurons. *Journal of Neuroscience*, 26(26):7035–7045, 2006.

[29] C.R. Noback, D.A. Ruggiero, R.J. Demarest, and N.L. Strominger. *The Human Nervous System: Structure and Function*. Springer e-Books. Humana Press, 2005.

[30] P. Matthews, P. Nathan, A. Loewy, G. Ratcliff, T. Lentz, and C.R. Noback. Human nervous system - The autonomic nervous system. https://www.britannica.com/science/human-nervous-system, 2019. (Accessed on 01/08/2020).

[31] G.A. Mihailoff and Duane Haines. *The Cell Biology of Neurons and Glia*, pages 15–33.e1. 01 2018.

[32] P. Brodal. *The Central Nervous System*. Oxford University Press, 2010.

[33] D. Purves. *Neuroscience*. Sinauer Associates, 2012.

[34] J.H. Caldwell. Action Potential Initiation and Conduction in Axons. *Encyclopedia of Neuroscience*, pages 23–29, 01 2010.

[35] Aviad Hai, Joseph Shappir, and Micha E. Spira. Long-Term, Multisite, Parallel, In-Cell Recording and Stimulation by an Array of Extracellular Microelectrodes. *Journal of Neurophysiology*, 104(1):559–568, 2010. PMID: 20427620.

[36] Marie Engelene J. Obien, Kosmas Deligkaris, Torsten Bullmann, Douglas J. Bakkum, and Urs Frey. Revealing neuronal function through microelectrode array recordings. *Frontiers in Neuroscience*, 8:423, 2015.

[37] Massimo Scanziani and Michael Häusser. Electrophysiology in the age of light. *Nature*, 461(7266):930–939, 2009.

[38] Peter Dayan and L. F. Abbott. *Theoretical Neuroscience: Computational and Mathematical Modeling of Neural Systems*. The MIT Press, 2005.

[39] Nobutaka Hirokawa, Shinsuke Niwa, and Yosuke Tanaka. Molecular motors in neurons: Transport mechanisms and roles in brain function, development, and disease. *Neuron*, 68(4):610–638, 2010.

[40] Katherine L. Gibbs, Linda Greensmith, and Giampietro Schiavo. Regulation of Axonal Transport by Protein Kinases. *Trends in Biochemical Sciences*, 40(10):597–610, 10 2015.

[41] Sandra Maday, Alison E. Twelvetrees, Armen J. Moughamian, and Erika L.F. Holzbaur. Axonal Transport: Cargo-Specific Mechanisms of Motility and Regulation. *Neuron*, 84(2):292–309, 2014.

[42] Anthony Brown, Lei Wang, and Peter Jung. Stochastic Simulation of Neurofilament Transport in Axons: The "Stop-and-Go" Hypothesis. *Molecular biology of the cell*, 16(9):4243–55, 10 2005.

[43] Pedro Guedes-Dias and Erika L.F. Holzbaur. Axonal transport: Driving synaptic function. *Science*, 366(6462), 2019.

[44] Yuyu Song and Scott T. Brady. Post-translational modifications of tubulin: Pathways to functional diversity of microtubules. *Trends in Cell Biology*, 25(3):125–136, 2015.

[45] Sumio Terada, Masataka Kinjo, Makoto Aihara, Yosuke Takei, and Nobutaka Hirokawa. Kinesin-1/Hsc70-dependent mechanism of slow axonal transport and its relation to fast axonal transport. *EMBO Journal*, 29(4):843–854, 2010.

[46] Amrita Mandal and Catherine M. Drerup. Axonal Transport and Mitochondrial Function in Neurons. *Frontiers in Cellular Neuroscience*, 13:373, 2019.

[47] Michal Cagalinec, Mailis Liiv, Zuzana Hodurova, Miriam Ann Hickey, Annika Vaarmann, Merle Mandel, Akbar Zeb, Vinay Choubey, Malle Kuum, Dzhamilja Safiulina, Eero Vasar, Vladimir Veksler, and Allen Kaasik. Role of Mitochondrial Dynamics in Neuronal Development: Mechanism for Wolfram Syndrome. *PLoS Biology*, 14(7):1–28, 2016.

[48] Tommy Lewis Jr, Gergely Turi, Seok-Kyu Kwon, Attila Losonczy, and Franck Polleux. Progressive Decrease of Mitochondrial Motility during Maturation of Cortical Axons In Vitro and In Vivo. *Current Biology*, 26, 09 2016.

[49] Geon Kim, Kanghyun Kim, Eunji Lee, Taechang An, WooSeok Choi, Geunbae Lim, and Jung Shin. Recent Progress on Microelectrodes in Neural Interfaces. *Materials*, 11:1995, 10 2018.

[50] Kristine Heiney, José C. Mateus, Cátia D.F. Lopes, Estrela Neto, Meriem Lamghari, and Paulo Aguiar. SpikeHunter: An advanced computational tool for the analysis of neuronal communication and action potential propagation in microfluidic platforms. *Scientific Reports*, 9(1):1–14, 2019.

[51] Anne Taylor, Mathew Blurton-Jones, Seog Rhee, David Cribbs, Carl Cotman, and Noo Jeon. A microfluidic culture platform for CNS axonal injury, regeneration and transport. *Nature methods*, 2:599–605, 09 2005.

[52] Multi Channel Systems. https://www.multichannelsystems.com/. (Accessed on 01/15/2020).

[53] Philipp Schätzle, Lukas C. Kapitein, and Casper C. Hoogenraad. Chapter 4 - Live imaging of microtubule dynamics in organotypic hippocampal slice cultures. In *The Neuronal Cytoskeleton, Motor Proteins, and Organelle Trafficking in the Axon*, volume 131 of *Methods in Cell Biology*, pages 107 – 126. Academic Press, 2016.

[54] Sylvia Neumann, Romain Chassefeyre, George Campbell, and Sandra Encalada. KymoAnalyzer: A Software Tool for the Quantitative Analysis of Intracellular Transport in Neurons: Axonal transport analysis using KymoAnalyzer. *Traffic*, 18, 2016.

[55] Maximilian Jakobs, Andrea Dimitracopoulos, and Kristian Franze. Kymobutler, a deep learning software for automated kymograph analysis. *eLife*, 8:e42288, 08 2019.

[56] Mengmeng Chen, Yang Li, Mengxue Yang, Xiaoping Chen, Yemeng Chen, Fan Yang, Sheng Lu, Shengyu Yao, Timothy Zhou, Jianghong Liu, Li Zhu, Sidan Du, and Jane Y. Wu. A new method for quantifying mitochondrial axonal transport. *Protein and Cell*, 7(11):804–819, November 2016.

[57] Cell Tracking Challenge. http://celltrackingchallenge.net/. (Accessed on 12/14/2019).

[58] Rangaraj M. Rangayyan. *Biomedical Image Analysis*. Biomedical Engineering. CRC Press, 2004.

[59] Pengyuan Li, Xiangying Jiang, Chandra Kambhamettu, and Hagit Shatkay. Compound image segmentation of published biomedical figures. *Bioinformatics*, 34(7):1192–1199, 10 2017.

[60] KTH-SE – Cell Tracking Challenge. http://celltrackingchallenge.net/participants/KTH-SE/. (Accessed on 12/17/2019).

[61] Johannes Schindelin, Ignacio Arganda-Carreras, Erwin Frise, Verena Kaynig, Mark Longair, Tobias Pietzsch, Stephan Preibisch, Curtis Rueden, Stephan Saalfeld, Benjamin Schmid, Jean Yves Tinevez, Daniel James White, Volker Hartenstein, Kevin Eliceiri, Pavel Tomancak, and Albert Cardona. Fiji: An open-source platform for biological-image analysis. *Nature Methods*, 9(7):676–682, 2012.

[62] Jean Yves Tinevez, Nick Perry, Johannes Schindelin, Genevieve M. Hoopes, Gregory D. Reynolds, Emmanuel Laplantine, Sebastian Y. Bednarek, Spencer L. Shorte, and Kevin W. Eliceiri. TrackMate: An open and extensible platform for single-particle tracking. *Methods*, 115:80–90, 2017.

[63] Shani Gluska, Michael Chein, Nimrod Rotem, Ariel Ionescu, and Eran Perlson. Chapter 18 - Tracking Quantum-Dot labeled neurotropic factors transport along primary neuronal axons in compartmental microfluidic chambers. In *The Neuronal Cytoskeleton, Motor Proteins, and Organelle Trafficking in the Axon*, volume 131 of *Methods in Cell Biology*, pages 365 – 387. Academic Press, 2016.

[64] Simon Andrews, Jonathan Gilley, and Michael P. Coleman. Difference Tracker: ImageJ plugins for fully automated analysis of multiple axonal transport parameters. *Journal of Neuroscience Methods*, 193(2):281–287, 2010.

[65] Cátia Lopes, Carla Gomes, Estrela Neto, Paula Sampaio, Paulo Aguiar, and Ana Paula Pego. Microfluidic-based platform to mimic the in vivo peripheral administration of neurotropic nanoparticles. *Nanomedicine*, 11, 11 2016.

[66] Chris Harris and Mike Stephens. A combined corner and edge detector. In *In Proc. of Fourth Alvey Vision Conference*, pages 147–151, 1988.

[67] Jianbo Shi and Carlo Tomasi. Good features to track. *IEEE Conference on Computer Vision and Pattern Recognition*, pages 593–600, 1994.

[68] J. Gibson and O. Marques. *Optical Flow and Trajectory Estimation Methods*. SpringerBriefs in Computer Science. Springer International Publishing, 2016.

[69] Bruce Lucas and Takeo Kanade. An Iterative Image Registration Technique with an Application to Stereo Vision (IJCAI). volume 81, 04 1981.

[70] Dhara M. Patel and Saurabh Upadhyay. Optical flow measurement using lucas kanade method. *International Journal of Computer Applications*, 61:6–10, 2013.

[71] J.-Y. Bouguet. Pyramidal implementation of the lucas kanade feature tracker. 1999.

[72] KymoResliceWide: ImageJ plugin making kymographs. https://github.com/ekatrukha/KymoResliceWide. (Accessed on 04/13/2020).

[73] Zhijia Zhang, Zelin Shi, Weifang Guo, and Shabai Huang. Adaptively image de-striping through frequency filtering. In Yunlong Sheng, Songlin Zhuang, and Yimo Zhang, editors, *ICO20: Optical Information Processing*, volume 6027, pages 989 – 996. International Society for Optics and Photonics, SPIE, 2006.

[74] Introduction to HDF5. https://portal.hdfgroup.org/display/HDF5/Introduction+to+HDF5. (Accessed on 06/03/2020).

[75] McsPy DataTools documentation. https://mcspydatatools.readthedocs.io/en/latest/index.html. (Accessed on 06/03/2020).

[76] Rodrigo Quian, Zoltan Nadasdy, and Yoram Ben-Shaul. Unsupervised Spike Detection and Sorting with Wavelets and Superparamagnetic Clustering. *Neural computation*, 16:1661–87, 09 2004.